JOURNAL OF PETROLOGY | VOLUME 38 | NUMBER 10 | PAGES 1359–1390 | 1997

Petrogenesis of Quaternary Intraplate Volcanism, Sana'a, Yemen: Implications for Plume–Lithosphere Interaction and Polybaric Melt Hybridization

J. A. BAKER*, M. A. MENZIES, M. F. THIRLWALL AND C. G. MACPHERSON

DEPARTMENT OF GEOLOGY, ROYAL HOLLOWAY UNIVERSITY OF LONDON, EGHAM, TW20 0EX, UK

RECEIVED JANUARY 2, 1997; REVISED TYPESCRIPT ACCEPTED JUNE 13, 1997

Quaternary intraplate volcanism near Sana'a, western Yemen, produced a chemically and isotopically diverse volcanic field. The predominantly mafic samples include alkali basalt, transitional basalt, basanite and trachybasalt; rarer evolved compositions are typically trachyandesite. No samples represent primary magmas, all having undergone fractionation of olivine + clinopyroxene ± plagioclase ± Fe–Ti oxides ± apatite. Sr–Nd–Pb–O isotopic variation ($^{87}Sr/^{86}Sr = 0{\cdot}7032$–$0{\cdot}7046$; $^{143}Nd/^{144}Nd = 0{\cdot}51298$–$0{\cdot}51278$; $^{206}Pb/^{204}Pb = 18{\cdot}93$–$18{\cdot}05$; $\delta^{18}O = +5{\cdot}2$ to $+5{\cdot}5‰$) is largely the result of mixing between a mantle component, with a composition intermediate between that of mid-ocean ridge basalt (MORB) and the Afar plume, and 0–20% of an Early Proterozoic or Late Archaean silicic lower-crustal component which produced little change in $\delta^{18}O$ values. Ratios of very to moderately incompatible trace elements vary widely (e.g. $Ce/Y = 0{\cdot}9$–$3{\cdot}7$) and independently of isotopic composition. Semi-quantitative modelling of REE ratios requires this heterogeneity to be the product of mixing between small melt fractions (<1%) from recently incompatible-trace-element-enriched garnet peridotite facies mantle and relatively larger melt fractions (~5%) from spinel peridotite facies mantle, with samples containing 40–90% spinel-facies melt. Substantial variations in Zr/Sm and Nb/La ratios also suggest that the spinel-facies mantle may be amphibole bearing. Intraplate volcanism in western Yemen appears to be the result of melting shallow mantle, perhaps in response to small amounts of lithospheric extension, that was metasomatized and hydrated by the Afar plume during, or shortly after, Oligocene flood volcanism.

KEY WORDS: *Yemen; intraplate volcanism; Sr–Nd–Pb isotopes; assimilation; Afar plume; partial melting*

INTRODUCTION

The ultimate source and reason(s) why continental intraplate volcanism occurs remain unclear, despite common links with continental rifting and regions of mantle upwelling. The extensive belt of late Cenozoic (<15 Ma) intraplate volcanic fields that crops out along the length of the western margin of the Arabian peninsula in Jordan, Israel, Saudi Arabia and Yemen forms one of the largest intraplate volcanic provinces on Earth. These volcanic rocks are generally more alkaline than older Eocene to Miocene flood volcanism erupted at the Afro-Arabian triple junction in Yemen, Ethiopia and Eritrea (Camp & Roobol, 1992). Intraplate volcanism in Yemen is clearly associated with both continental rifting, which produced the Red Sea and Gulf of Aden, and also a mantle plume, which produced Oligocene flood volcanism (Baker *et al.*, 1996). Given the well-characterized crustal and mantle (asthenospheric, plume and lithospheric mantle) compositions in this region, Yemen is an ideal setting in which to attempt to identify the source of intraplate volcanism and to speculate on why it occurred during the Late Cenozoic.

Detailed chemical, but not isotopic, studies of some of the Saudi Arabian volcanic fields have been published (Camp & Roobol, 1989; Camp *et al.*, 1991, 1992), highlighting the role of fractional crystallization and variable degrees of partial melting in generating the diversity of predominantly mafic rock types present in these fields.

*Corresponding author. Telephone: +44 (0) 1784 443631. Fax: +44 (0) 1784 471780. e-mail: joel@gl.rhbnc.ac.uk

Stein & Hofmann (1992) and Altherr *et al.* (1990) presented a substantial amount of isotopic data for intraplate volcanic rocks from Israel and throughout the Arabian peninsula, respectively. Both studies concluded that the primary magmas were derived from a shallow mantle source, with Stein & Hofmann (1992) speculating that the common isotopic signature of the intraplate basalts is consistent with derivation from material emplaced below the continental lithosphere by a mantle plume(s). However, all of the aforementioned studies are essentially reconnaissance studies that did not provide both chemical and isotopic data for a single intraplate volcanic field.

This paper presents detailed chemical and isotopic data for a single intraplate volcanic field located in western Yemen, near Sana'a, which is one of four such intraplate volcanic fields in Yemen that post-date Oligocene flood volcanism (Fig. 1; Manetti *et al.*, 1991; Cox *et al.*, 1993). Only with these data is it possible to assess rigorously the roles of fractional crystallization, mantle source heterogeneity, and variable depths and degrees of partial melting in the formation of these rocks and, subsequently, to speculate on the nature of the source and reasons why post-flood volcanic intraplate magmatism occurred in Yemen.

FIELD GEOLOGY

Quaternary intraplate volcanism north of Sana'a covers an area of ~800 km^2 (Fig. 2) and, although laterally extensive, is only a thin carapace (<200 m) with an estimated volume of 60 ± 20 km^3. This is the volumetric equivalent of about five Oligocene flood basalt flows in this region, and some two orders of magnitude smaller than the total volume of preserved flood volcanism in Yemen (Baker, 1996). Quaternary volcanism is associated with an area of inland drainage referred to as the Sana'a basin, which is infilled with Plio-Quaternary sedimentary rocks. This depression may be a small extensional basin or graben. Similar associations of crustal depressions and intraplate magmatism are observed elsewhere on the Arabian peninsula, e.g. Harrat Kishb (Camp *et al.*, 1992).

The volcanic field comprises a number of sub-horizontal lava flows each 5–20 m thick unconformably overlying Jurassic–Cretaceous Amran and Tawilah Group sedimentary rocks (Davison *et al.*, 1994), and in some places Oligocene flood volcanic flows. The volcanic plateau is peppered by Strombolian ash and spatter cones and a small number of stratovolcanoes (e.g. Jabals Zin and Al Hamudi).

The volcanism can be divided into four phases on the basis of relative age and morphological relationships: (1) the sub-horizontal, plateau-forming basalt flows; (2) at least two large stratovolcanoes which erupted the most evolved compositions in the entire volcanic field; (3) some 60 scoria cones, 20–500 m high, constructed by a combination of Strombolian- to Hawaiian-type eruptions; (4) a number of aa-type lava flows, up to 15 km long, that were fed from parasitic vents around the base of the ash and spatter cones (3), some of which were erupted between AD 200 and 500 and clearly post-date historical settlement (Ambraseys *et al.*, 1994).

To assess any temporal geochemical variability in the composition of the volcanic rocks, samples were collected from a variety of volcanic features in varying degrees of morphological degradation (Fig. 2). As far as possible, sampling also sought to encompass the entire geographical extent of the volcanic field, although this was limited by a number of military and communications bases located in this region, near which access is prohibited.

On the basis of morphology there is a clear distinction in relative age between the older plateau-forming flows and the large stratovolcanoes, and the considerably better preserved Strombolian ash and spatter cones with their parasitic Recent lava flows. This distinction is used to divide the volcanic samples into two suites, an old and young series, in later geochemical discussions. No geochronological data are available for the oldest units in the Sana'a volcanic field. However, the morphology of the field, coupled with the unconformable lower contact with underlying eroded pre-Miocene sedimentary and volcanic rocks, and the lack of significant unconformities or disconformities within the various volcanic units, suggests that it is predominantly of Plio-Quaternary age.

ANALYTICAL TECHNIQUES

Major and trace element and Sr–Nd–Pb–O isotopic data for the intraplate volcanic rocks are given in Tables 1 and 2. Major and most trace element data were determined on fused glass discs and pressed powder pellets, respectively, by X-ray fluorescence (XRF) spectrometry at Royal Holloway University of London (RHUL). Analytical reproducibility of XRF major and trace element data presented in Table 1 is better than (± 2 SD): SiO_2 $\pm 0{\cdot}3$ wt %; Al_2O_3 $\pm 0{\cdot}1$ wt %; Fe_2O_3 $\pm 0{\cdot}05$ wt %; MgO $\pm 0{\cdot}10$ wt %; CaO $\pm 0{\cdot}05$ wt %; Na_2O $\pm 0{\cdot}1$ wt %; K_2O $\pm 0{\cdot}004$ wt %; TiO_2 $\pm 0{\cdot}01$ wt %; MnO $\pm 0{\cdot}01$ wt %; P_2O_5 $\pm 0{\cdot}01$ wt %; Ni ± 1 p.p.m.; Cr $\pm 1{\cdot}5$ p.p.m.; V $\pm 1{\cdot}5$ p.p.m.; Sc $\pm 0{\cdot}8$ p.p.m.; Cu $\pm 1{\cdot}5$ p.p.m.; Zn ± 1 p.p.m.; Cl ± 20 p.p.m.; Ga $\pm 0{\cdot}9$ p.p.m.; Pb $\pm 0{\cdot}5$ p.p.m.; Sr ± 2 p.p.m.; Rb $\pm 0{\cdot}5$ p.p.m.; Ba ± 5 p.p.m.; Zr ± 1 p.p.m.; Nb $\pm 0{\cdot}5$ p.p.m.; Th $\pm 0{\cdot}4$ p.p.m.; Y $\pm 0{\cdot}6$ p.p.m.; La ± 2 p.p.m.; Ce ± 2 p.p.m.; Nd ± 1 p.p.m. At high trace element concentration levels reproducibility increases to $\pm 1\%$. Pb and Th were determined using extended count times and calibrated against a set of international and in-house standards with

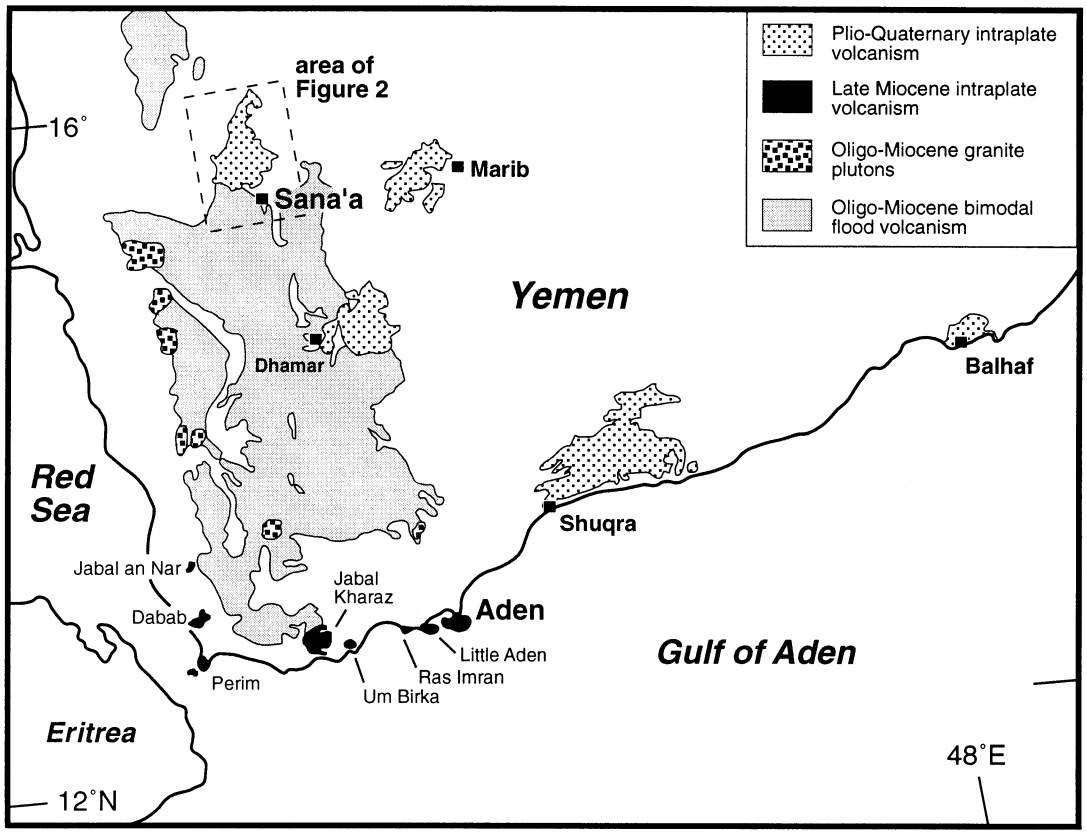

Fig. 1. Distribution of Oligo-Miocene flood volcanism, and Late Miocene and Plio-Quaternary intraplate volcanism in Yemen. Late Miocene volcanoes are primarily concentrated along the southern coast of Yemen. The main Plio-Quaternary volcanic fields all fall to the east of the main Oligo-Miocene flood volcanic field. Modified after Manetti *et al.* (1991).

Pb and Th determined by isotope dilution (Pb) and neutron activation (Th) analysis. The rare earth elements (REE) and U were determined on a subset of samples by thermal ionization mass spectrometric isotope dilution analysis, with <0·5% and <1% reproducibility on REE and U contents, respectively.

Sr, Nd and Pb isotopic compositions were determined, after chemical separation using cation (Sr) and anion exchange resins (Nd–Pb), on a VG354 multicollector mass spectrometer at RHUL. Sample powders for Sr isotope analysis were leached in hot 6 M HCl for 1 h and repeatedly rinsed in ultraclean water before dissolution. Sr and Nd isotope analyses were determined in multi-dynamic mode as outlined by Thirlwall (1991). In-run internal precision of Sr and Nd isotope analyses was better than $\pm$0·000012 and $\pm$0·000006, respectively (2 SE). External precision or reproducibility of Sr and Nd isotopic data is better than $\pm$0·000018 and $\pm$0·000013 (n>50; 2 SD) and ratios are reported relative to values of 0·710250 for SRM987 and 0·511424 for an in-house laboratory Nd standard. This Nd isotopic ratio corresponds to 0·511860 and 0·512638 for the international standards La Jolla and BCR-1, respectively. Pb isotopic data, collected in static multicollector mode, were normalized for mass fractionation by comparison with repeated analyses of SRM981. Normalizing factors for $^{206}Pb/^{204}Pb$, $^{207}Pb/^{204}Pb$ and $^{208}Pb/^{204}Pb$ were 1·00267, 1·00335 and 1·00528, corresponding to mass fractionation of 1·33‰, 1·12‰ and 1·31‰ per a.m.u., respectively. External precision of SRM981 shows that reproducibility of sample Pb isotope analyses is approximately $\pm$0·010, $\pm$0·012 and $\pm$0·030 (2 SD) for $^{206}Pb/^{204}Pb$, $^{207}Pb/^{204}Pb$ and $^{208}Pb/^{204}Pb$, respectively, significantly more than the typical within-run precision (2 SE) of $\pm$0·004, $\pm$0·004 and $\pm$0·007. Total procedural blanks for the Sr, Nd and Pb separation procedure were approximately 1·5, 0·3 and 0·5 ng, respectively, and are negligible. The young age of the intraplate volcanic samples precludes the need for an age correction to the radiogenic isotopic data.

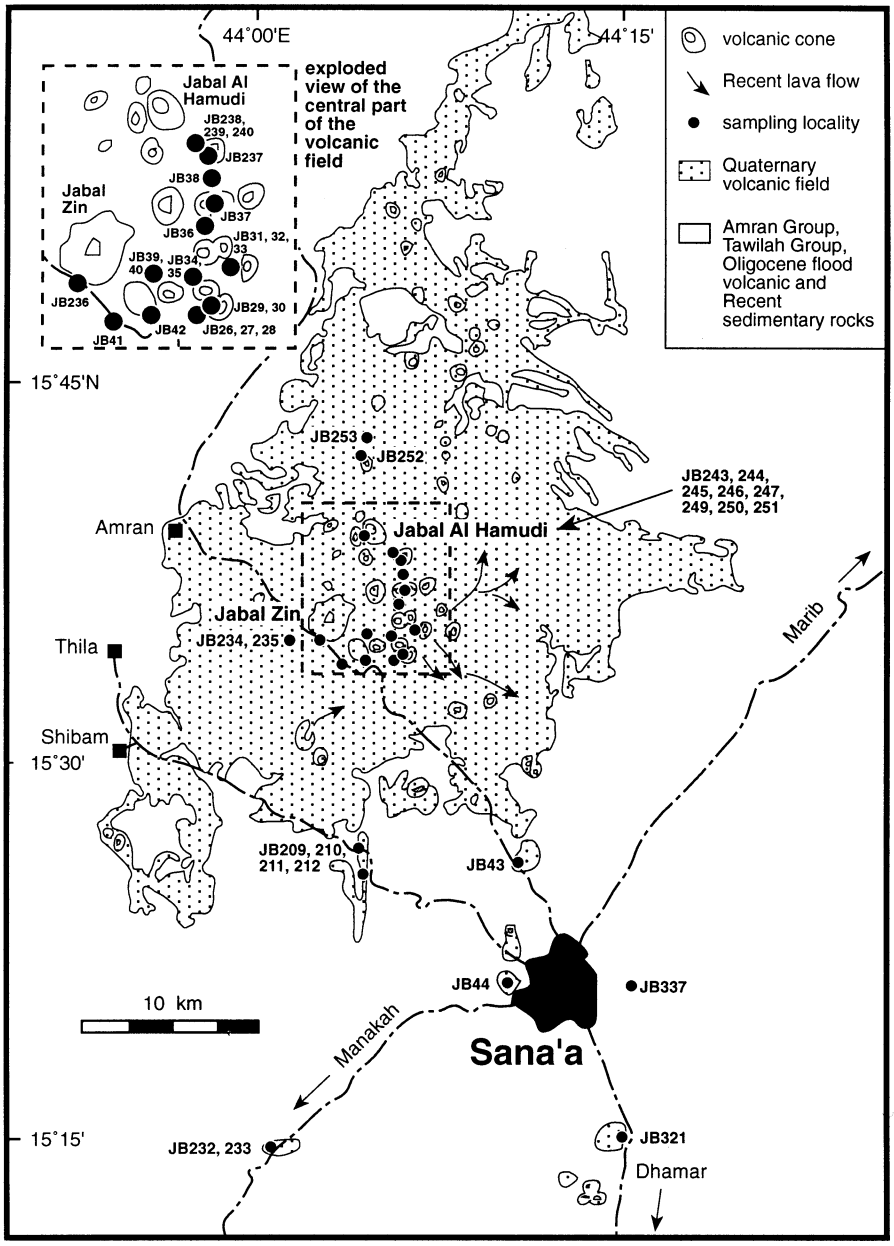

Fig. 2. Distribution of Plio-Quaternary volcanism in the Sana'a–Amran volcanic field, showing the main sampling locations. More outcrops of Quaternary volcanism occur to the south of the main volcanic field than are illustrated in this figure, but it is difficult to distinguish these from fresh outcrops of Oligocene flood basalt. Compiled from Kruck (1983), aerial photographs and field mapping.

Oxygen isotopic determinations were made on 1–2 mg of hand-picked olivine crystals using the laser fluorination technique of Mattey & Macpherson (1993) at RHUL. All oxygen yields were $100 \pm 2\%$. Replicate analyses of in-house standards (e.g. SC olivine $= 4{\cdot}86 \pm 0{\cdot}16$‰), and duplicate analyses of half the samples, suggests that precision on $\delta^{18}O$ values is $\leq 0{\cdot}15$‰ (2 SD). The mean value determined on this line for the NBS28 quartz standard by laser heating an SC olivine and NBS28 quartz mix is $9{\cdot}57 \pm 0{\cdot}36$‰ ($n = 17$; D. Lowry, unpublished data, 1996).

PETROGRAPHY

All of the samples studied are porphyritic, and contain 5–30 modal % of unaltered olivine (ol), plagioclase (plag) and clinopyroxene (cpx) phenocrysts. However, the

Table 1: Major and trace element data for Quaternary intraplate volcanic rocks, Sana'a, western Yemen

Sample no.:	JB29	JB30	JB33	JB36	JB37	JB40	JB41	JB42	JB209	JB210	JB211	JB233	JB234	JB235	JB236
wt %															
SiO_2	45·8	47·2	46·8	48·6	48·7	47·8	46·5	48·2	48·4	48·8	51·3	46·7	49·0	46·6	58·9
Al_2O_3	16·1	16·4	16·5	16·6	16·9	16·2	16·2	16·2	16·7	17·0	16·8	16·0	16·4	15·9	15·6
Fe_2O_3	11·96	11·23	11·96	12·13	11·93	10·85	11·36	10·58	11·35	12·79	12·27	11·61	11·84	11·33	11·01
MgO	8·28	7·78	7·75	6·42	5·40	7·46	8·30	7·66	6·40	4·27	3·18	8·77	7·12	9·59	0·86
CaO	9·47	8·90	8·42	7·96	8·96	9·77	9·16	9·29	9·22	7·03	5·96	9·48	8·11	9·81	3·42
Na_2O	3·99	4·35	4·42	4·53	4·07	3·42	4·05	3·85	3·57	4·48	5·08	3·20	4·10	3·59	5·26
K_2O	0·865	1·042	0·987	0·895	1·037	1·075	0·991	0·921	1·067	1·605	1·963	1·051	0·783	0·651	3·096
TiO_2	2·33	2·17	2·21	1·90	2·25	1·97	2·06	1·99	2·20	2·61	1·71	2·18	1·77	2·09	0·85
MnO	0·185	0·180	0·184	0·209	0·202	0·174	0·186	0·185	0·194	0·211	0·242	0·187	0·204	0·180	0·255
P_2O_5	0·56	0·58	0·56	0·68	0·55	0·64	0·45	0·54	0·54	0·97	0·87	0·50	0·50	0·39	0·38
Total	99·52	99·83	99·71	100·00	99·94	99·43	99·20	99·48	99·66	99·73	99·42	99·64	99·82	100·12	99·60
mg-no.	0·58	0·58	0·56	0·51	0·47	0·58	0·59	0·59	0·53	0·40	0·34	0·60	0·54	0·63	0·13
LOI (wt %)	−0·34	−0·61	−0·54	−0·61	0·08	1·67	−0·44	−0·02	0·35	−0·02	−0·79	−0·37	−0·31	−0·50	−0·17
p.p.m.															
Ni	120	115	116	96	45	153	121	134	51	10	12	161	145	172	4
Cr	179	206	145	149	93	294	190	347	121	7	6	261	253	341	2
V	209	196	212	154	336	183	217	197	231	151	69	237	180	227	5
Sc	25·1	24·8	24·0	23·7	30·1	23·3	24·9	26·8	26·3	16·5	12·9	27·6	24·9	29·7	32·1
Cu	64	56	60	75	44	58	54	59	39	26	23	63	61	77	12
Zn	78	77	77	82	98	77	75	75	86	91	100	76	83	70	153
Cl	304	330	256	453	154	146	417	416	59	308	120	421	92	319	80
Ga	15·3	16·6	16·9	17·4	20·0	17·5	17·5	15·7	18·5	18·3	20·0	16·0	16·7	16·0	29·8
Pb	1·7	2·2	1·9	1·7	2·6	3·3	2·1	2·5	2·8	4·1	3·5	1·9	1·7	1·2	10·0
Sr	775	700	710	486	463	721	593	543	497	696	599	532	437	507	322
Rb	17·2	22·0	19·1	17·0	19·6	18·7	21·1	19·5	21·0	35·0	42·9	24·7	16·9	13·8	67·0
Ba	294	332	306	255	313	449	332	310	382	614	669	387	268	212	1071
Zr	201	234	210	275	268	231	183	275	225	245	351	175	283	203	797
Nb	37·4	42·2	36·2	31·3	29·3	39·0	39·5	39·2	35·4	73·1	81·8	51·9	28·6	28·5	76·5
Th	2·6	3·9	3·1	2·3	3·8	4·1	3·5	4·2	3·5	6·6	8·3	4·6	3·0	2·7	9·0
Y	32·2	30·4	29·6	38·3	44·1	32·0	28·2	33·1	33·7	32·7	41·7	26·6	37·8	29·9	90·6
La	33	33·5	30	25·6	29	40	29·4	33·1	32·0	55·0	62	36·3	27	22·7	83
Ce	72	69·4	64	58·7	63	80	59·4	70·4	66·9	109·0	123	71·8	59	52·9	171
Nd	36	33·8	31	32·3	34	40	28·2	34·4	33·4	48·0	54	32·4	32	28·2	83

Table 1: continued

Sample no.:	JB239	JB244	JB245	JB246	JB250	JB247	JB249	JB251	JB252	JB253	JB337	JB26	JB27	JB28	JB31
wt %															
SiO_2	45·9	48·0	48·7	48·0	46·4	48·4	46·2	46·9	46·3	46·6	48·2	50·4	46·3	45·7	47·0
Al_2O_3	16·2	16·8	17·2	17·0	17·3	16·9	17·1	16·9	16·0	16·4	16·3	17·2	16·0	16·2	16·4
Fe_2O_3	11·66	12·89	12·19	12·70	11·96	11·82	12·30	12·22	11·17	10·84	10·91	12·29	11·52	12·09	11·53
MgO	7·54	6·10	6·56	5·31	7·14	6·41	7·33	7·26	8·90	9·50	7·24	3·67	8·23	8·51	8·07
CaO	9·08	8·51	8·52	7·75	10·15	8·71	9·44	9·54	9·77	11·40	8·64	6·70	9·06	9·28	8·70
Na_2O	4·41	3·91	3·79	3·93	3·09	3·92	3·11	3·35	3·73	2·66	4·22	4·67	4·18	4·15	3·98
K_2O	1·228	0·745	0·748	1·225	0·815	0·872	0·779	0·508	0·729	0·354	1·169	1·913	0·966	0·861	1·145
TiO_2	2·41	2·10	1·84	2·31	2·50	2·03	2·61	2·27	2·03	1·51	2·07	2·21	2·05	2·52	2·23
MnO	0·186	0·210	0·204	0·206	0·193	0·205	0·194	0·198	0·176	0·176	0·184	0·207	0·188	0·186	0·184
P_2O_5	0·72	0·57	0·52	0·66	0·48	0·59	0·46	0·34	0·56	0·25	0·68	0·88	0·63	0·51	0·68
Total	99·31	99·79	100·27	99·10	100·00	99·86	99·47	99·46	99·36	99·76	99·62	100·08	99·10	99·97	99·86
mg-no.	0·56	0·48	0·52	0·45	0·54	0·52	0·54	0·54	0·61	0·64	0·57	0·37	0·59	0·58	0·58
LOI (wt %)	−0·29	−0·11	−0·29	−0·02	0·35	−0·10	−0·06	−0·48	−0·57	−0·46	−0·29	0·00	−0·27	−0·70	−0·12
p.p.m.															
Ni	91	48	53	23	50	66	60	62	147	176	98	10	137	119	118
Cr	157	60	68	21	62	95	117	100	268	393	184	8	231	168	184
V	203	173	170	178	262	172	288	251	216	243	182	118	199	220	202
Sc	24·0	26·3	25·2	23·7	27·7	22·8	29·2	30·7	28·5	35·6	23·5	16·1	26·0	25·3	24·7
Cu	60	44	40	33	40	63	43	48	68	115	55	28	67	65	59
Zn	87	96	99	105	77	81	76	78	73	72	79	88	81	70	88
Cl	371	13	17	54	212	23	244	6	215	18	739	98	472	308	536
Ga	17·1	18·6	19·3	19·3	17·7	17·0	16·9	17·2	16·1	16·8	17·0	18·2	16·3	16·0	17·1
Pb	1·1	2·9	2·5	3·4	1·7	2·3	1·5	1·2	1·6	0·6	3·1	4·9	2·0	0·6	2·8
Sr	921	433	441	524	587	557	550	470	597	352	742	656	703	758	877
Rb	23·5	12·2	11·8	21·5	15·2	17·6	15·6	7·5	13·7	5·4	23·7	47·6	18·6	16·6	22·7
Ba	408	304	321	536	279	336	264	214	237	128	430	699	314	285	399
Zr	235	301	302	260	227	283	217	170	198	120	241	292	221	186	211
Nb	49·6	23·5	24·1	41·4	38·2	40·6	36·4	20·9	25·5	12·4	43·0	91·6	40·2	34·8	50·4
Th	3·8	2·4	2·3	3·6	3·8	4·4	3·3	2·1	2·1	1·7	4·8	9·5	3·1	3·0	3·8
Y	31·0	48·1	44·3	40·7	32·7	38·0	32·1	33·7	30·6	27·1	32·5	35·6	29·2	31·0	29·1
La	42·0	24·6	27	38	30	36	27	18	22·5	10	41·1	70	33	31	40
Ce	86·4	57·9	61	78	65	73	57	43	49·4	23	82·6	132	70	66	83
Nd	41·0	35·0	35	39	32	36	30	24	27·2	15	38·2	53	34	34	40

Table 1: continued

Sample no.:	JB32	JB34	JB35	JB38	JB39	JB43	JB44	JB212	JB232	JB237	JB238	JB240	JB243	JB321	Mean
wt %															
SiO_2	47·6	46·7	45·9	47·4	47·9	47·9	47·1	49·6	48·0	46·1	46·4	46·2	48·6	46·6	47·7
Al_2O_3	16·7	16·2	16·3	16·4	16·6	16·4	16·4	17·0	17·7	16·2	16·3	16·2	17·1	16·2	16·5
Fe_2O_3	11·70	11·46	11·92	11·47	11·42	11·13	11·16	12·50	11·03	11·61	11·76	11·65	11·95	11·47	11·68
MgO	7·11	8·47	8·27	7·42	7·11	7·56	8·02	4·44	6·09	7·45	7·62	7·32	5·48	7·36	6·95
CaO	8·26	9·05	9·48	8·53	8·51	8·69	8·77	7·16	9·12	8·92	9·08	8·92	8·70	8·90	8·68
Na_2O	4·46	4·12	4·15	4·65	4·34	3·99	4·45	4·25	3·38	4·58	4·44	4·46	4·16	4·58	4·09
K_2O	1·083	0·964	0·903	1·095	1·096	1·177	1·130	1·557	1·111	1·229	1·232	1·355	0·837	1·355	1·11
TiO_2	2·24	2·22	2·52	2·11	2·10	2·22	2·19	2·03	2·47	2·40	2·46	2·57	2·06	2·57	2·17
MnO	0·187	0·179	0·177	0·179	0·185	0·181	0·180	0·234	0·176	0·189	0·195	0·183	0·205	0·183	0·19
P_2O_5	0·57	0·52	0·55	0·61	0·65	0·56	0·66	0·76	0·43	0·72	0·73	0·65	0·53	0·73	0·59
Total	99·86	99·87	100·12	99·87	99·88	99·77	100·11	99·54	99·53	99·44	100·22	99·48	99·51	99·90	99·71
mg-no.	0·55	0·59	0·58	0·56	0·55	0·57	0·59	0·41	0·52	0·56	0·56	0·55	0·48	0·56	0·53
LOI (wt %)	−0·26	0·22	−0·28	0·03	−0·37	−0·20	−0·55	−0·46	−0·07	−0·60	−0·40	−0·58	−0·10	−0·68	−0·25
p.p.m.															
Ni	94	130	112	103	96	103	114	25	45	91	90	82	85	88	89
Cr	141	201	156	187	175	162	179	21	65	150	157	130	158	141	151
V	185	136	217	191	180	196	192	134	244	199	212	213	208	219	196
Sc	23·4	26·5	25·9	23·7	22·8	24·9	23·4	17·3	23·1	23·0	23·8	22·5	26·3	23·6	24·7
Cu	50	48	61	50	48	57	59	40	37	63	60	62	43	66	53
Zn	76	76	74	81	84	73	74	96	62	83	89	85	80	84	83
Cl	360	273	414	404	357	382	448	62	4	592	599	667	8	494	286
Ga	15·6	16·6	15·3	17·5	17·9	17·5	18·3	18·7	16·0	17·2	17·9	18·7	16·8	17·4	17·6
Pb	2·3	1·0	2·0	2·6	2·3	3·0	1·8	2·6	1·8	1·9	2·2	2·9	3·2	2·8	2·5
Sr	690	681	782	678	753	645	785	591	704	916	937	941	544	935	655
Rb	21·1	19·0	17·8	21·9	22·1	24·8	23·6	32·7	25·3	24·2	24·7	25·2	14·9	24·2	22·3
Ba	348	304	287	350	408	366	380	557	394	408	414	432	339	456	385
Zr	228	204	193	227	223	211	211	283	161	234	238	236	248	224	243
Nb	41·5	36·5	36·1	39·8	43·5	42·1	43·8	68·4	47·5	48·9	50·9	49·5	36·3	46·5	43·1
Th	3·1	2·9	3·6	4·0	4·3	4·4	4·0	5·8	4·2	3·8	4·0	3·9	3·6	3·9	4·0
Y	30·9	30·7	31·8	31·5	31·9	31·6	29·7	38·6	23·7	31·3	31·4	30·2	38·0	30·2	34·3
La	33	31	31	32	39	33	36	49	35	42	45	39	31	39	36
Ce	68	66	68	65	78	72	72	98	71	85	92	79	63	82	75
Nd	34	33	34	32	36	35	35	45	32	41	43	39	33	40	37

Table 2: U and REE isotope dilution and Sr–Nd–Pb–O isotopic data for Quaternary intraplate volcanic rocks, Sana'a, western Yemen

Sample no.:	JB29	JB30	JB33	JB36	JB37	JB40	JB41	JB42	JB209	JB210	JB211	JB233	JB234
p.p.m.													
U	0·776	0·822	—	0·556	—	—	0·718	0·826	0·717	1·262	0·899	0·955	—
La	—	33·5	—	25·6	—	—	29·4	33·1	32·0	55·0	—	36·3	—
Ce	—	69·4	—	58·7	—	—	59·4	70·4	66·9	109·0	—	71·8	—
Nd	—	33·8	—	32·3	—	—	28·2	34·4	33·4	48·0	—	32·4	—
Sm	—	6·87	—	7·06	—	—	5·82	6·91	6·84	8·56	—	6·14	—
Eu	—	2·26	—	2·35	—	—	1·95	2·22	2·19	2·71	—	1·96	—
Gd	—	6·54	—	6·95	—	—	5·74	6·75	6·54	7·39	—	5·61	—
Dy	—	5·37	—	6·62	—	—	5·01	5·85	5·77	6·00	—	4·70	—
Er	—	2·85	—	3·86	—	—	2·69	3·23	3·29	3·38	—	2·62	—
Yb	—	2·52	—	3·53	—	—	2·40	2·97	2·96	2·77	—	2·27	—
Lu	—	0·36	—	0·53	—	—	0·35	0·44	0·44	0·41	—	0·33	—
$^{87}Sr/^{86}Sr$	0·70333	0·70325	0·70338	0·70327	0·70360	0·70349	0·70340	0·70349	0·70404	0·70378	0·70352	0·70360	0·70328
$^{143}Nd/^{144}Nd$	0·512963	0·512971	—	0·512977	—	—	0·512946	0·512922	0·512835	0·512828	0·512908	0·512870	—
ε_{Nd}	6·18	6·34	—	6·45	—	—	5·85	5·38	3·69	3·55	5·11	4·37	—
$^{206}Pb/^{204}Pb$	18·663	18·765	—	18·509	—	—	18·715	18·731	18·378	18·715	18·727	18·756	—
$^{207}Pb/^{204}Pb$	15·535	15·617	—	15·546	—	—	15·594	15·603	15·603	15·617	15·603	15·567	—
$^{208}Pb/^{204}Pb$	38·541	38·946	—	38·410	—	—	38·784	38·804	38·543	38·887	38·808	38·675	—
$\Delta 7/4$	2·1	9·2	—	4·9	—	—	7·4	8·2	12·0	9·7	8·2	4·3	—
$\Delta 8/4$	35·0	63·2	—	40·6	—	—	53·1	53·1	69·7	63·4	54·0	37·2	—
$\delta^{18}O$ (olivine)	—	5·21	—	—	—	—	5·28	—	5·36	5·51	—	5·34	—

Table 2: continued

Sample no.:	JB235	JB236	JB239	JB244	JB245	JB246	JB250	JB247	JB249	JB251	JB252	JB253	JB337
p.p.m.													
U	0·557	—	1·063	0·422	—	—	—	—	0·561	—	0·478	0·165	1·152
La	22·7	—	42·0	24·6	—	—	—	—	—	—	22·5	—	41·1
Ce	52·9	—	86·4	57·9	—	—	—	—	—	—	49·4	—	82·6
Nd	28·2	—	41·0	35·0	—	—	—	—	—	—	27·2	—	38·2
Sm	5·81	—	7·97	8·16	—	—	—	—	—	—	6·03	—	7·42
Eu	1·95	—	2·57	2·60	—	—	—	—	—	—	2·03	—	2·44
Gd	—	—	7·27	8·60	—	—	—	—	—	—	6·10	—	—
Dy	—	—	5·82	8·10	—	—	—	—	—	—	5·47	—	5·74
Er	—	—	2·93	4·76	—	—	—	—	—	—	2·99	—	3·15
Yb	2·65	—	2·53	4·35	—	—	—	—	—	—	2·71	—	2·67
Lu	—	—	0·37	0·62	—	—	—	—	—	—	—	—	—
$^{87}Sr/^{86}Sr$	0·70326	0·70463	0·70350	0·70349	0·70352	0·70388	0·70340	0·70331	0·70345	0·70363	0·70342	0·70337	0·70345
$^{143}Nd/^{144}Nd$	0·512970	0·512777	0·512924	0·512911	0·512899	0·512835	—	—	0·512952	0·512926	0·512940	0·512962	0·512930
ε_{Nd}	6·32	2·56	5·42	5·17	4·93	3·69	—	—	5·97	5·46	5·73	6·16	5·54
$^{206}Pb/^{204}Pb$	18·798	18·052	18·685	18·135	18·148	—	—	—	18·930	18·413	18·505	18·518	18·660
$^{207}Pb/^{204}Pb$	15·578	15·608	15·544	15·578	15·583	—	—	—	15·602	15·576	15·560	15·561	15·575
$^{208}Pb/^{204}Pb$	38·781	38·347	38·600	38·243	38·261	—	—	—	38·956	38·489	38·497	38·570	38·627
$\Delta 7/4$	4·9	16·0	2·8	12·1	12·5	—	—	—	5·9	8·9	6·3	6·3	6·1
$\Delta 8/4$	42·7	89·5	38·3	69·1	69·3	—	—	—	44·3	60·1	49·7	55·5	44·0
$\delta^{18}O$ (olivine)	—	—	5·24	5·27	5·52	—	—	—	—	5·47	5·39	5·19	5·30

phenocrysts are generally rather small (<1 mm) and no samples appear to be accumulative. Although most samples are ol + plag-phyric, with plagioclase a more abundant phenocryst phase in more evolved samples, there is no clear correlation between rock type and which samples are cpx-phyric. Fe–Ti oxides are a common phenocryst phase in the most evolved samples (MgO<6–7 wt %), with apatite (ap) also present as phenocrysts in trachyandesite JB236.

Although most samples contain subhedral to euhedral phenocrysts of ol + plag ± cpx that are normally zoned, some samples contain rare larger crystals of anhedral pink cpx (JB237 and JB239) and/or resorbed plagioclase crystals with later overgrowths.

Groundmass textures are holocrystalline with a seriate texture or cryptocrystalline. Larger and less vesiculated flows are characterized by coarser-grained groundmasses and, where identifiable, the groundmass mineralogy invariably includes plag + cpx + Fe–Ti oxides ± ol ± ap.

MAJOR AND TRACE ELEMENT CHEMISTRY

Chemical classification

Apart from one sample (JB236; trachyandesite) all of the samples have SiO_2 <52 wt % and can be classified as basanite (4), trachybasalt (21), basalt (16) and basaltic trachyandesite (2) (Le Bas *et al.*, 1986). Basalt samples include both nepheline- and hypersthene-normative compositions, i.e. alkali basalt (14) and basalt (2) *sensu stricto*.

Subdivision of the samples into two subsets on the basis of relative age reveals some marked chemical differences between the younger and older series. The younger series includes a greater proportion of more silica-undersaturated and alkaline (basanite and trachybasalt) rocks than the older series.

The Sana'a volcanic field is chemically similar to Saudi Arabian fields of the same age, but does not have abundant highly silica-undersaturated rocks as found in some Saudi Arabian fields (e.g. basanite to phonolite series—Harrat Kishb; Camp *et al.*, 1992).

Major element chemistry

MgO contents vary from 9·6 to 0·9 wt %, although all but the trachyandesite sample have MgO >3·2 wt %. Plots of MgO versus other major elements show the following trends with decreasing MgO (Fig. 3): (1) increasing SiO_2, Na_2O and K_2O in all samples; (2) increasing Al_2O_3, Fe_2O_3 and P_2O_5 in all samples except for those with MgO <4 wt %; (3) decreasing CaO and CaO/Al_2O_3 (not shown); (4) near-constant TiO_2 until MgO ~4 wt %, with a marked decrease in TiO_2 at lower MgO contents.

Two further features are evident from Fig. 3. First, it is clear that the younger series has a more restricted range in, and generally higher, MgO contents than the older series of samples. Second, the higher alkalinity of the young series is mirrored by generally higher Na_2O, K_2O and P_2O_5 contents, at the same MgO content, when compared with most of the old series.

Trace element chemistry

Bivariate MgO–trace element diagrams

Plots of MgO versus trace element data display the following trends with decreasing MgO (Fig. 4): (1) decreasing Ni, Cr, Sc and V abundances; (2) increasing large ion lithophile element (LILE; with the exception of Sr), high field strength element (HFSE), REE, Y, Th and U abundances. The MgO–Sr plot exhibits much scatter, which is a feature shared by many of the trace element plots, although there is a marginal increase in Sr abundances with decreasing MgO within each sample series. A feature of the MgO–Sr plot which is also exhibited by other very incompatible trace elements (VICE; i.e. LILE, Nb, LREE, Th, U) is the generally higher abundances of these trace elements in the young series compared with the old series at a specific MgO content.

Multielement diagrams

REE patterns of all samples are strongly light REE (LREE) enriched relative to chondrites [La = (70–200) × chondrite]. All samples are marked by a significant flattening of REE patterns from Dy to Lu compared with the LREE to medium REE (MREE) (Fig. 5). However, the heavy REE (HREE) part of the pattern is actually not flat and is enriched to some extent in the lighter HREE. Most high-MgO samples have small positive Eu anomalies (Eu/Eu* ~1·03; Fig. 5a), whereas some of the more evolved samples have negative Eu anomalies (Eu/Eu* ~0·96; Fig. 5b). An important feature of the REE data is that patterns for different samples cross, reflecting varying LREE/HREE ratios. It is clearly difficult to relate such samples by fractional crystallization of the phenocryst assemblage observed in these rocks.

Primitive-mantle-normalized multielement diagrams again highlight the wide range of VICE abundances relative to moderately incompatible elements (MICE) in these rocks that is not simply related to changing MgO

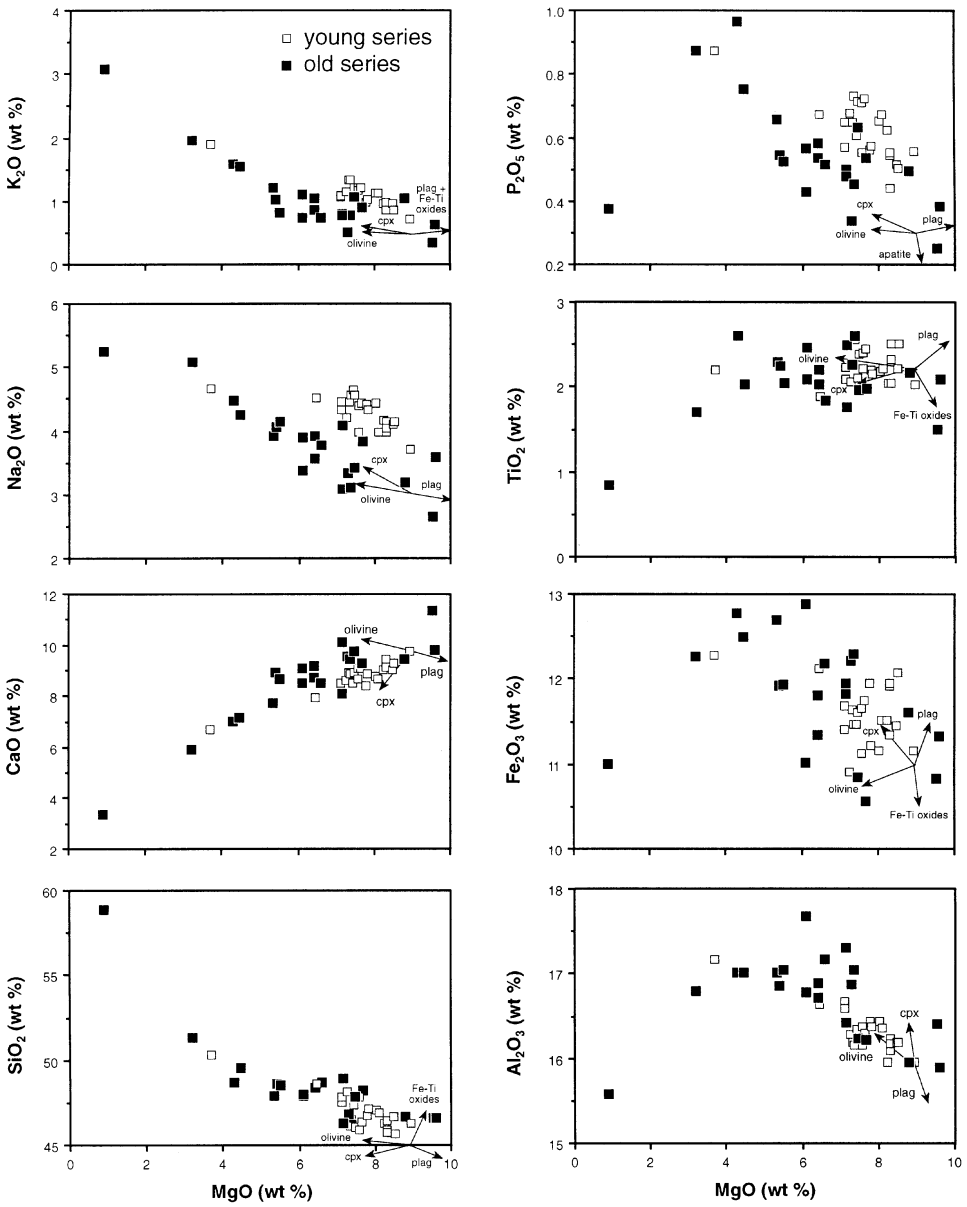

Fig. 3. MgO vs major element data; Sana'a Quaternary volcanic rocks. Selected diagrams are annotated with appropriate crystal fractionation vectors. ■, old series; □, young series.

content (Fig. 5c). Patterns for mafic samples peak at Nb with marked negative K, Th, U and Rb anomalies. Evolved samples often have more spiky multielement patterns which peak at Ba rather than Nb, have larger negative Th, U and Rb anomalies relative to Ba, smaller negative K anomalies compared with mafic samples, small positive Pb anomalies relative to Ce, and negative Sr and Ti anomalies (Fig. 5d). Mafic samples have multielement patterns similar to some ocean-island basalts (OIB, e.g. St Helena; Fig. 5c).

Sr–Nd–Pb–O ISOTOPE CHEMISTRY

Sr–Nd isotopic composition

Samples with SiO_2 <52 wt % have $^{87}Sr/^{86}Sr$ ratios that vary from 0·7032 to 0·7040 (Table 2; Fig. 6a). The trachyandesite sample extends this range to 0·7046. Similarly, $^{143}Nd/^{144}Nd$ ratios range from 0·51298 to 0·51283, with the trachyandesite having a markedly lower ratio of 0·51278. Sr and Nd isotopic ratios are strongly correlated (Fig. 6a).

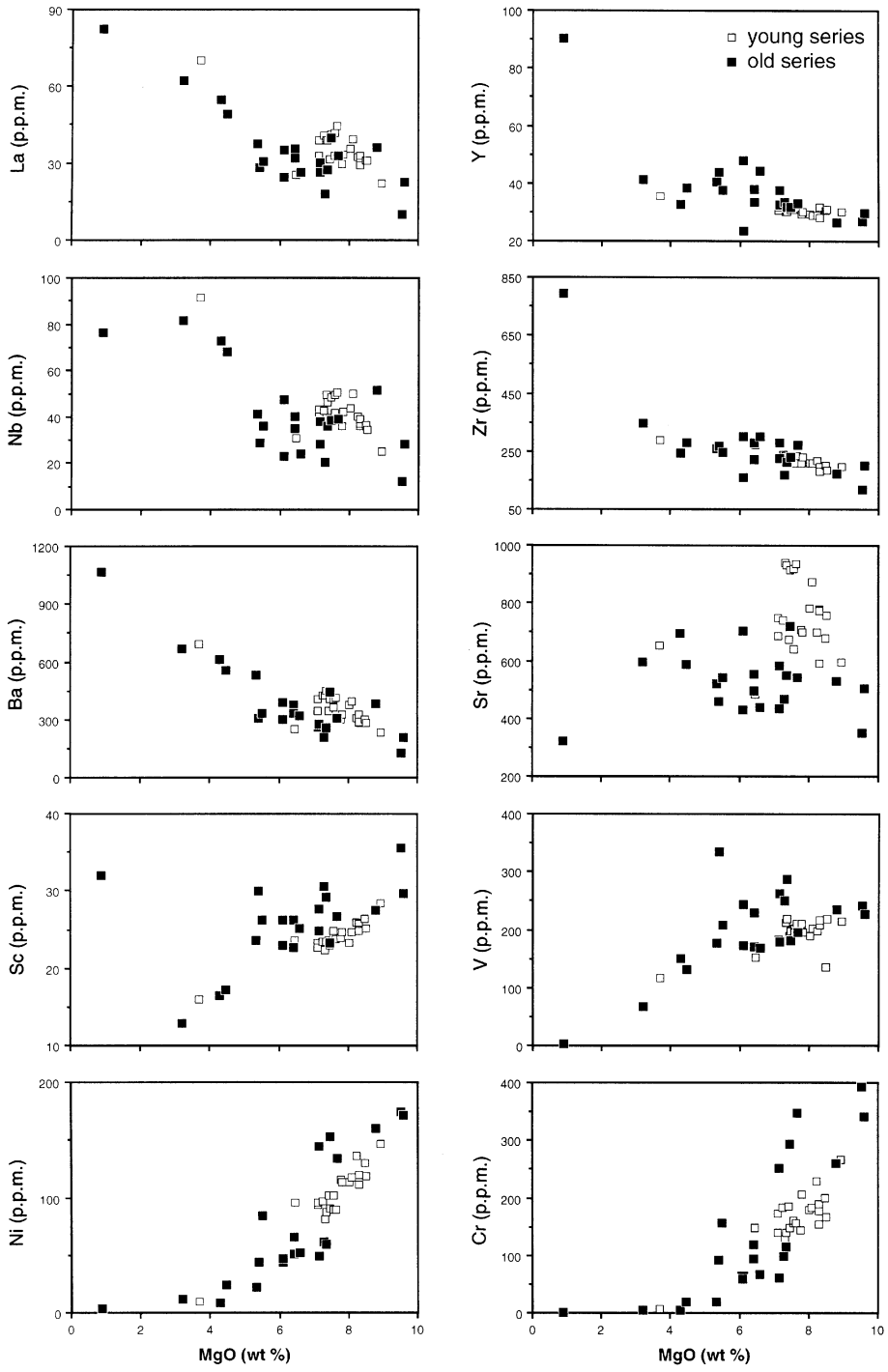

Fig. 4. MgO versus selected trace element data; Sana'a Quaternary volcanic rocks. Same symbols as in Fig. 3.

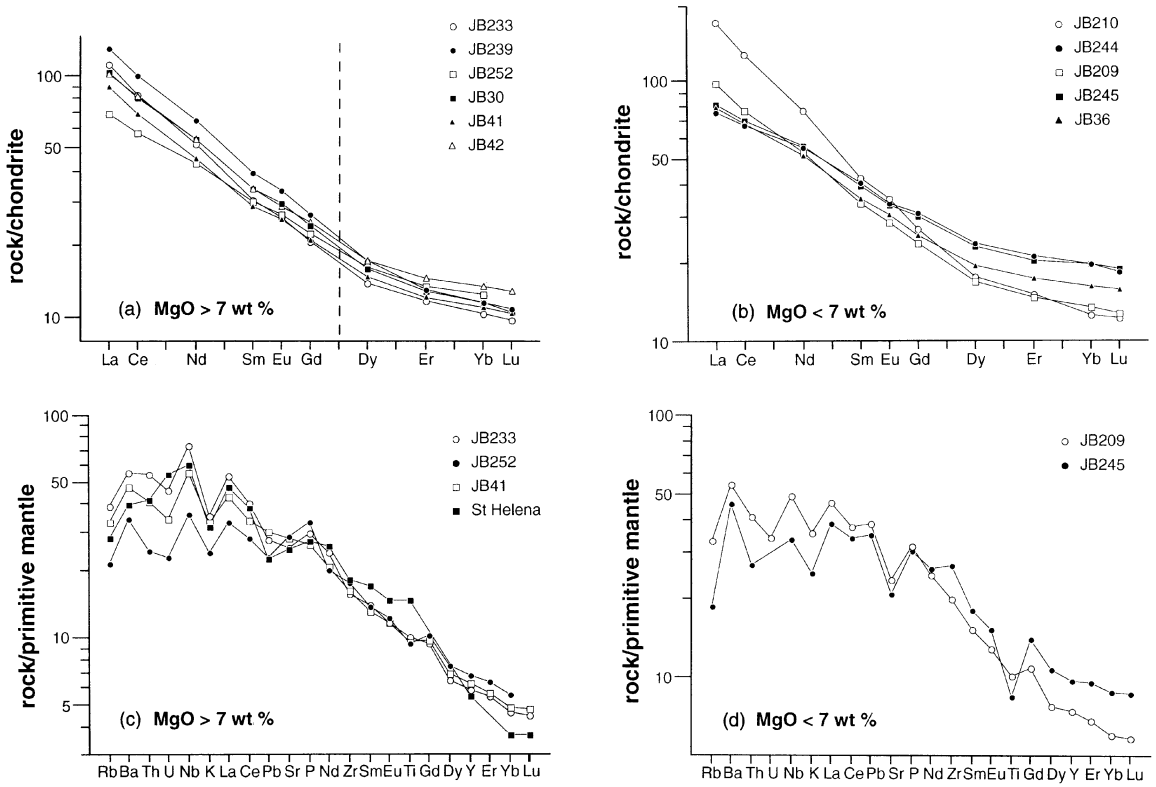

Fig. 5. Chondrite-normalized REE and primitive-mantle-normalized multielement diagrams for representative Sana'a samples. (a) and (c), primitive samples with MgO >7 wt %. A St Helena ocean-island basalt (OIB) has a similar multielement pattern to the primitive intraplate basalts (data from Chaffey *et al.*, 1989; M. F. Thirlwall, unpublished data, 1994). (b) and (d), evolved samples with MgO <7 wt %. Normalization values from: chondrites—Nakamura (1974); primitive mantle—Sun & McDonough (1989).

Sr–Nd isotopic data for possible mantle source compositions, and Cenozoic intraplate volcanic rocks erupted elsewhere in this region (Altherr *et al.*, 1990; Henjes-Kunst *et al.*, 1990; Schilling *et al.*, 1992; Volker *et al.*, 1993; J. A. Baker, unpublished data, 1996) are also compared with the Sana'a volcanic rocks in Fig. 6a. The Sana'a data set is characterized by a tighter Sr–Nd isotopic array than other Arabian intraplate volcanic rocks and, although it overlaps the field defined by these rocks, extends to higher $^{87}Sr/^{86}Sr$ and lower $^{143}Nd/^{144}Nd$ ratios. Many of the Arabian intraplate basalts have lower $^{87}Sr/^{86}Sr$ ratios than the Sana'a intraplate samples, a feature which is shared by Phanerozoic (200–1 Ma) alkali intraplate basalts from Israel (Stein & Hofmann, 1992).

Compared with fields defined for local MORB (Red Sea and Gulf of Aden ridges) and the lithospheric mantle (LM), the Sana'a samples clearly extend to more enriched isotopic compositions (Fig. 6a; MORB—Schilling *et al.*, 1992; Volker *et al.*, 1993; LM—Henjes-Kunst *et al.*, 1990; Blusztajn *et al.*, 1995; Baker, 1996). However, the Sana'a samples do overlap the isotopic composition attributed to the Afar plume on the basis of studies of the Gulf of Aden ridge (Schilling *et al.*, 1992), Recent intraplate volcanism in Djibouti (Vidal *et al.*, 1991; Deniel *et al.*, 1994) and Oligocene flood volcanism in Yemen (Baker *et al.*, 1996). Amphibole $\pm$ apatite-bearing LM xenoliths from south-western Yemen (Ataq) also have Sr and Nd isotopic ratios identical to this Afar plume signature (Fig. 6a; Baker, 1996). The Sana'a samples do, however, extend to marginally more depleted compositions than that defined for the Afar plume, to compositions that are intermediate between the MORB and Afar plume fields.

Crustal rocks from this region define a large field in Sr–Nd isotopic space (Fig. 6b), with isotopic compositions governed by the age and nature of the crust. Clearly, a number of these crustal components might be suitable end-members to generate the observed array in Sr–Nd isotopic space by crustal contamination processes. Recent Nd isotopic studies of basement rocks in Yemen have also delineated a series of crustal terranes of widely varying age, and hence isotopic composition (0·7–3·0 Ga; Windley *et al.*, 1996), with the Sana'a intraplate magmas erupted close to the inferred boundary of the Afif Terrane (0·7–2·4 Ga; depleted mantle Nd model ages of equivalent Saudi Arabian samples; Agar *et al.*, 1992) and the Abas Gneiss Terrane (1·7–2·3 Ga; depleted

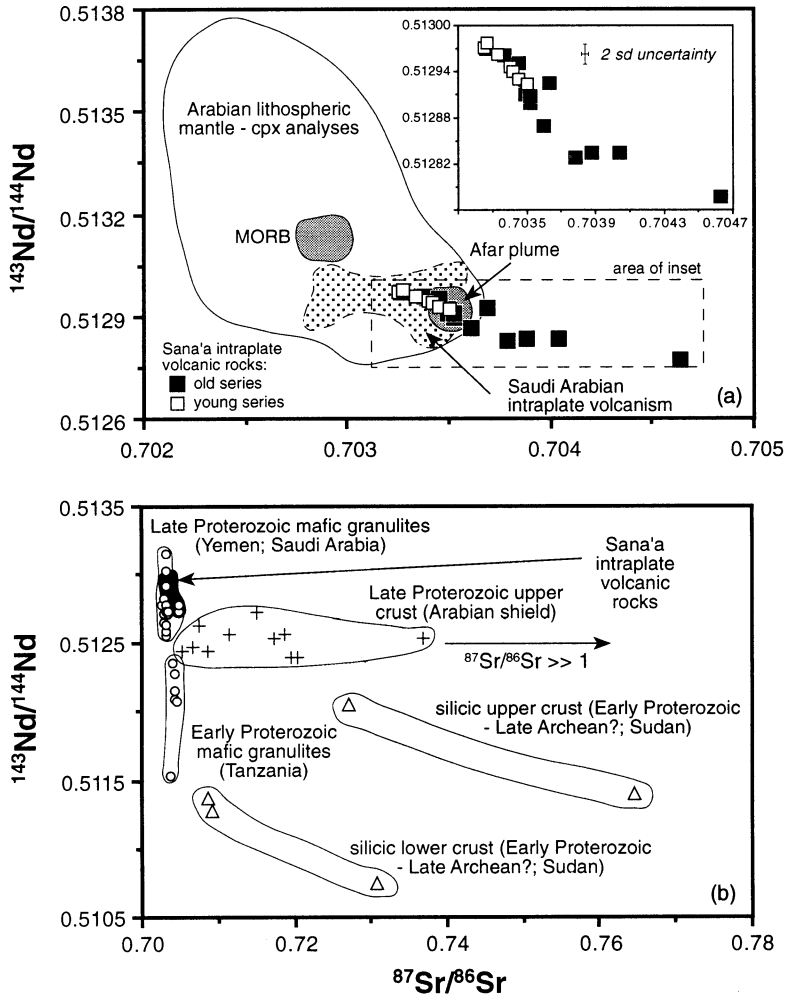

Fig. 6. Sr–Nd isotopic composition of the Sana'a volcanic rocks. (a) Compared with fields for MORB, the Afar plume, Arabian lithospheric mantle (LM), and Saudi Arabian intraplate volcanism. Data sources: MORB—Schilling *et al.* (1992) and Volker *et al.* (1993); Afar plume—Vidal *et al.* (1991), Schilling *et al.* (1992), Deniel *et al.* (1994); LM—Henjes-Kunst *et al.* (1990) and J. A. Baker (unpublished data, 1996); Saudi Arabian intraplate volcanism—Altherr *et al.* (1990). (b) Compared with typical crustal compositions in this region. Data sources: Sudan—Davidson & Wilson (1989); Early Proterozoic mafic granulites—Cohen *et al.* (1984); Late Proterozoic mafic granulites—McGuire & Stern (1993) and G. Chazot & J. A. Baker (unpublished data, 1996); Late Proterozoic upper crust (Saudi Arabia)—Duyverman *et al.* (1982) and Hegner & Pallister (1989).

mantle Nd model ages of Yemeni samples; Windley *et al.*, 1996).

Pb isotopic composition

The Pb isotopic composition of the Sana'a samples varies markedly, e.g. $^{206}Pb/^{204}Pb = 18{\cdot}05–18{\cdot}93$ (Fig. 7a). In plots of $^{207}Pb/^{204}Pb$ and $^{208}Pb/^{204}Pb$ vs $^{206}Pb/^{204}Pb$ the samples form a scattered field that extends from close to the fields defined by the Afar plume, Ataq LM xenoliths and Saudi Arabian intraplate volcanism to lower $^{206}Pb/^{204}Pb$ and $^{208}Pb/^{204}Pb$ ratios at a relatively constant $^{207}Pb/^{204}Pb$ ratio (Fig. 7a and b). None of the samples fall within the field defined for local MORB mantle.

A more detailed examination of Fig. 7a and b could lead to the interpretation that the scattered field of data might actually define three linear trends in Pb isotopic space emanating from a common $^{206}Pb/^{204}Pb$ ratio of ~18·65. One trend (group 1) extends to unradiogenic Pb, whereas the other two trends extend towards more radiogenic Pb isotopic compositions with different trajectories (groups 2 and 3). Although the group 2 and 3 trends in the $^{207}Pb/^{204}Pb$ vs $^{206}Pb/^{204}Pb$ plot are close to mass fractionation trajectories, the co-variation in $^{208}Pb/^{204}Pb$ precludes these apparent trends being a function of mass fractionation. A plot of $\Delta 7/4$ vs $\Delta 8/4$ (Fig. 7c) provides important constraints on the nature of the Pb isotopic variability. The Sana'a samples define a linear

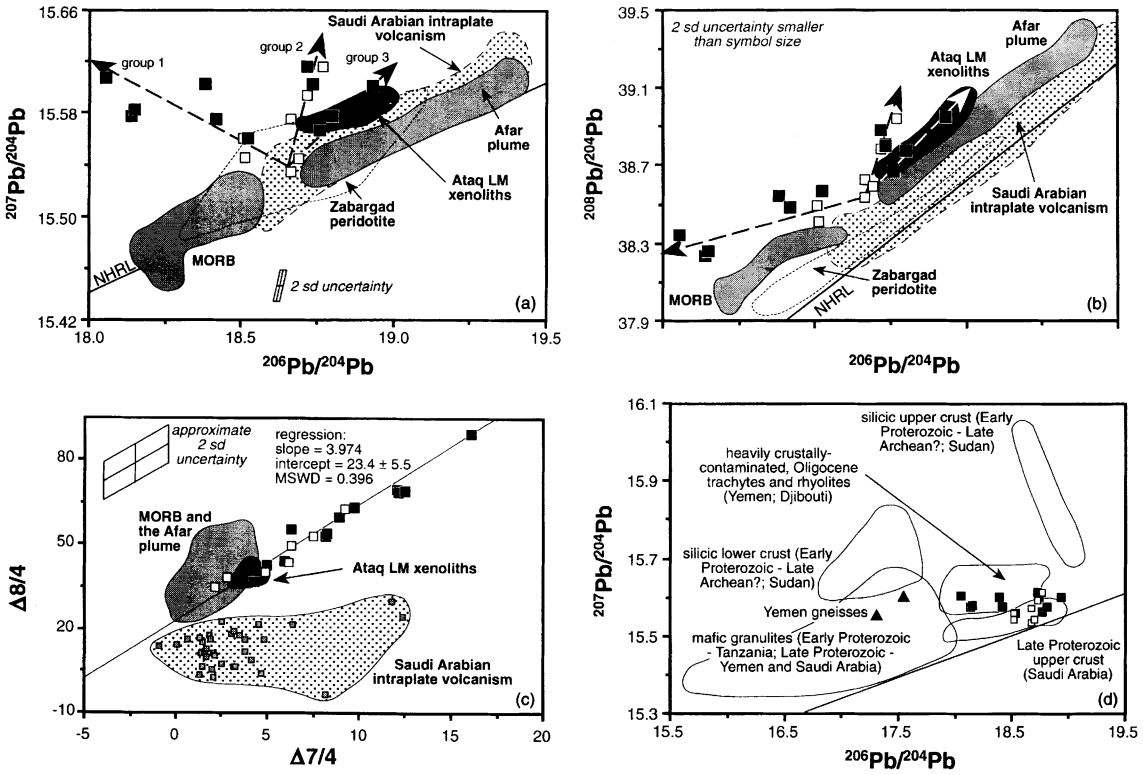

Fig. 7. (a) and (b), Pb isotopic composition of Sana'a volcanic rocks compared with other volcanic and LM compositions in the Red Sea, Gulf of Aden, and Arabian peninsula. Data sources: MORB—Schilling *et al.* (1992) and Volker *et al.* (1993); Afar plume—Vidal *et al.* (1991) and Deniel *et al.* (1994); Saudi Arabian intraplate volcanic rocks—Altherr *et al.* (1990), excluding two samples with very high Δ7/4; Zabargad peridotite—Hamelin & Allègre (1988); Ataq peridotites—J. A. Baker (unpublished data, 1996). (c) Δ7/4 vs Δ8/4 for Sana'a volcanic rocks compared with other volcanic compositions in the Red Sea, Gulf of Aden and Arabian peninsula region. Data sources are the same as for Fig. 6a. (d) Pan-African crustal Pb isotope compositions. Crustal data sources: Late Proterozoic Saudi Arabian upper crust—Hegner & Pallister (1989); Sudanese crust—Davidson & Wilson (1989); mafic granulites—Cohen *et al.* (1984), Altherr *et al.* (1990) and G. Chazot & J. A. Baker (unpublished data, 1995); Yemen gneiss samples (J. A. Baker, unpublished data, 1997); crustally contaminated Oligocene silicic volcanic rocks—Deniel *et al.* (1994) and Baker (1996). NHRL, Northern Hemisphere Reference Line.

array in this plot which extends from the MORB–Afar plume and Ataq LM xenolith field towards a component with high Δ7/4 and Δ8/4. The key feature of this plot is that the linear array allows the Pb isotopic variability to be explained by mixing between two components, with the component close to the Northern Hemisphere Reference Line (NHRL) and mantle fields having slightly variable Pb isotope ratios but constant Δ7/4 and Δ8/4.

Thus, one component has a variable Pb isotopic composition ($^{206}Pb/^{204}Pb = 18{\cdot}65–19{\cdot}25$) and lies sub-parallel to the NHRL with $\Delta7/4 = +2$ and $\Delta8/4 = +30$. This component is most closely represented by the 'group 3' samples, has relatively restricted $^{87}Sr/^{86}Sr$ (Fig. 8) and $^{143}Nd/^{144}Nd$ ratios, and lies very close to the Afar plume field and analyses of amphibole, clinopyroxene and apatite separated from LM xenoliths entrained in Quaternary alkali basalt lavas from southern Yemen (Ataq; Baker, 1996). Importantly, the linear array of data in the Δ7/4 vs Δ8/4 plot (Fig. 7c) confirms the general observation from the $^{206}Pb/^{204}Pb$ vs $^{208}Pb/^{204}Pb$ plot that Saudi Arabian intraplate volcanism has lower Δ8/4 values than the Sana'a samples (Fig. 7b). The Zabargad peridotite is also marked by lower Δ8/4 values than the Sana'a samples (Fig. 7b).

The second component has a composition most closely approximated by the trachyandesite sample and lies close to published analyses of Early Proterozoic to Late Archaean silicic lower crust from Sudan (Fig. 7d; Davidson & Wilson, 1989), and two garnetiferous gneiss samples collected from ~50 km east of Sana'a (Fig. 7d; J. A. Baker, unpublished data, 1997). Compilation of crustal Pb isotopic data from this region clearly illustrates that a younger Late Proterozoic crustal component, similar to that encountered in much of Saudi Arabia,

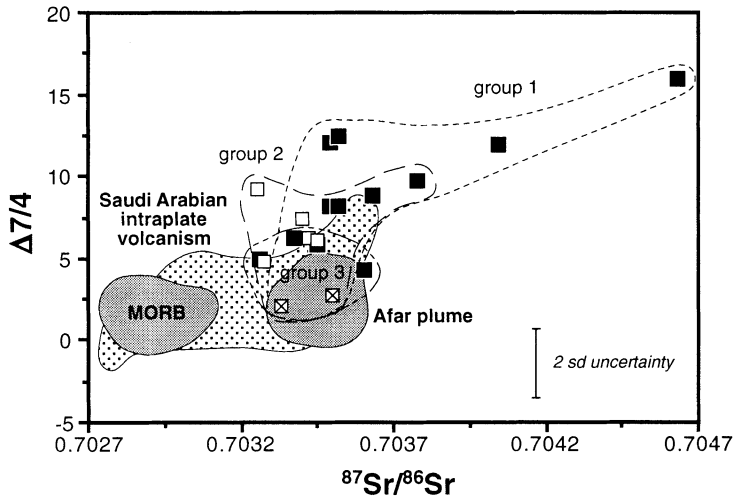

Fig. 8. Co-variation of $^{87}Sr/^{86}Sr$ with Δ7/4. Three groups of data from the Sana'a volcanic field are circled on the basis of the apparent trends in Fig. 7. The two open symbols with crosses inside are the samples which fall closest to the NHRL. Data sources are the same as for Figs 6 and 7.

could not be responsible for the trend to unradiogenic Pb.

O isotopic composition

$\delta^{18}O$ values of olivine separated from 12 samples vary from +5·2 to +5·5‰ (Table 2). The range of olivine oxygen isotope compositions from the intraplate samples overlaps that defined for mantle peridotites by the same technique ($\delta^{18}O = +5{\cdot}18 \pm 0{\cdot}28$‰; Mattey *et al.*, 1994), but extends to marginally higher values. However, the range of volcanic olivine values (0·3‰) is similar to the assessed analytical reproducibility of the laser fluorination technique.

DISCUSSION

The Sana'a samples have *mg*-numbers and Cr and Ni contents too low for these rocks to represent primary magmas (e.g. Roeder & Emslie, 1970; Hart & Davis, 1978). Significant variations in VICE abundances and VICE/MICE ratios characterize samples with the same MgO content, and a subset of samples exhibit significant Sr–Nd–Pb isotopic heterogeneity. The following discussion considers the petrogenetic processes that may have produced these features either *en route* to the surface or during partial melting of the mantle source, i.e. fractional crystallization, crustal contamination, variable depths and degrees of partial melting and mantle heterogeneity.

Fractional crystallization

Petrographic observations suggest that ol + plag may have been important fractionating phases in all the Sana'a volcanic rocks. Fe–Ti oxides ± apatite may also have been important fractionating phases at lower MgO contents (<6 wt %) and, although phenocrysts of clinopyroxene are present in only 25% of the samples, it may have also been a fractionating mineral.

Qualitative observations

Differentiation trends (Fig. 3) are consistent with fractionation of ol + plag + cpx ± Fe–Ti oxides ± apatite having played a role, at some stage, in generating the major element variation observed in these rocks. Marked decreases in MgO and Ni (Figs 3 and 4) require olivine fractionation throughout the fractionation sequence.

Plagioclase fractionation was certainly important in the more evolved rocks (MgO <6 wt %), and resulted in relatively constant or decreasing Sr abundances, especially in the older sample suite. Moreover, two further features also support the involvement of plagioclase fractionation. First, decreases in Sr/Nd ratios and development of small negative Eu anomalies in samples with MgO <7 wt % (Fig. 5) are consistent with plagioclase fractionation. Second, increasing Fe_2O_3 in all but the most evolved samples cannot be achieved by fractionation of ol ± cpx ± Fe–Ti oxides alone and also necessitates the fractionation of a non-Fe-bearing mineral, i.e. plagioclase. However, increasing Al_2O_3 with decreasing MgO until MgO <5 wt % suggests that plagioclase was not the principal fractionating phase during the early stages of magmatic differentiation.

Although fractionating ol + plag could generate the decline in CaO observed with decreasing MgO, this is again inconsistent with the increase in Al_2O_3 observed with decreasing MgO in all but the most evolved samples. Thus, this decrease in CaO also requires significant clinopyroxene fractionation throughout the fractionation sequence, and is consistent with decreases in Cr, V and Sc abundances and CaO/Al_2O_3 ratios observed with decreasing MgO.

Decreases in Fe_2O_3 and TiO_2 in the most evolved samples (MgO <4–6 wt %) requires fractionation of an Fe–Ti oxide phase. A more rapid decrease in V abundances observed at these MgO contents is also consistent with the onset of Fe–Ti oxide fractionation. A marked decrease in P_2O_5 in the most evolved (trachyandesite) samples was the result of late-stage apatite fractionation.

In summary, qualitative examination of major and trace element data apparently indicates a requirement for fractional crystallization of ol + cpx throughout the fractionation sequence, with plagioclase also a significant fractionating phase at MgO <7–8 wt %. Fe–Ti oxides joined the fractionating assemblage at MgO ~5 wt %, and apatite also began to fractionate at MgO <4 wt %.

Quantitative modelling of fractional crystallization

Major elements. Numerous attempts were made to model the major element chemical variation observed in the Sana'a volcanic suite. Least-squares major element mixing calculations were undertaken using a variety of selected parent and daughter samples, the mineral phases identified above, and a variety of appropriate mineral compositions. Despite attempting a large number of models incorporating a wide range of mineral compositions and selecting parent–daughter samples with similar VICE/MICE and isotopic ratios, most calculated models typically yielded rather poor fits with large residuals for SiO_2, Na_2O, K_2O and TiO_2 and a sum of the squared residuals, Σr^2, >1. Some of the better models indicated that the observed major element variation at high MgO contents (>7 wt %) may be a function of almost sub-equal ol + cpx fractionation with variable, and subordinate, amounts of plagioclase fractionation. At lower MgO contents the models that gave a better fit indicated that plagioclase becomes an important fractionating phase, with titanomagnetite and apatite also fractionating. In these respects, at least, the least-squares mixing models concurred with the conclusions drawn from qualitative examination of the major and trace element variations.

Trace elements. Almost without exception, the trace element modelling failed to reproduce closely the observed daughter trace element abundances using realistic mineral–melt partition coefficients (Baker, 1996). Many of the VICE abundances calculated for hypothetical daughter samples lie 10–50% outside the observed daughter values. These discrepancies are not simply a function of the choice of distribution coefficients, as observed enrichments for some sample pairs exceed that possible even if the bulk distribution coefficients are taken as zero (Baker, 1996).

Summary

Although qualitative observations require fractional crystallization of ol + cpx + plag ± Fe–Ti oxides ± apatite in the Sana'a intraplate magmas, considerable shortcomings in this hypothesis were exposed by quantitative modelling of major and trace element variations (Baker, 1996). The reasons for this are twofold. First, the Sana'a intraplate magmas may have undergone high-pressure and/or polybaric fractionation; the Sana'a samples plot away from the 1 bar ol + cpx + plag cotectic defined by Sack *et al.* (1987) towards higher-pressure cotectics (Fig. 9). High-pressure and/or polybaric fractionation is consistent with the presence of corroded pink clinopyroxene crystals in some samples that may be the remnants of higher-pressure aluminous clinopyroxene phenocrysts. Second, later in this paper, the failure of quantitative major and trace element fractionation modelling is shown to predominantly reflect the effects of other petrogenetic processes, particularly crustal contamination, variable degrees of partial melting and mantle heterogeneity, rather than more complex crystallization processes or fractionation of minerals not observed as phenocrysts in the intraplate volcanic rocks.

Crustal contamination vs mantle heterogeneity

Isotopic and incompatible trace element components contributing to intraplate volcanism

Sr–Nd–Pb isotopic data indicate that at least two components contributed to the petrogenesis of the Sana'a volcanic rocks (Figs 6 and 7). Samples with low $^{87}Sr/^{86}Sr$ and high $^{143}Nd/^{144}Nd$ ratios generally have the lowest $\Delta 7/4$ (e.g. Fig. 8) and $\Delta 8/4$ values and may reflect a component that lies close to the data fields defined by the Afar plume and Ataq LM xenoliths. This component apparently had some Pb isotopic variability, and possibly also some limited Sr–Nd isotopic variation (e.g. Fig. 8), but is marked by constant $\Delta 7/4$ and $\Delta 8/4$ values (Fig. 7c).

Samples with enriched Sr–Nd isotopic compositions have unradiogenic Pb and high $\Delta 7/4$ (Fig. 8) and $\Delta 8/4$ values that extend towards analyses of silicic lower crust from Sudan and gneisses from western Yemen; these samples define a second component involved in the petrogenesis of the magmas.

Some incompatible trace element ratios also correlate with isotopic composition. Samples with unradiogenic

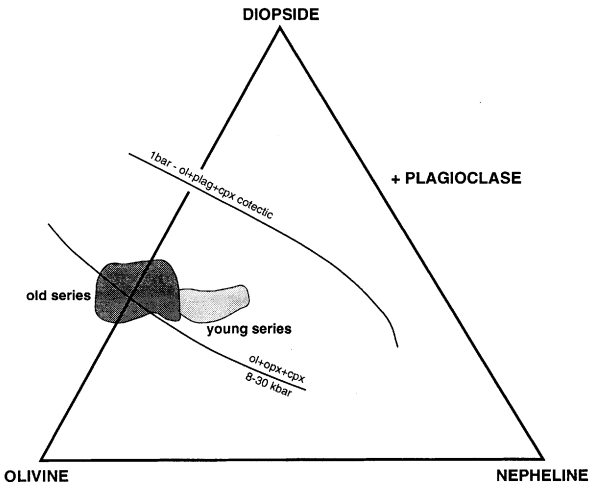

Fig. 9. Normative olivine–diopside–nepheline phase diagram illustrating that the Sana'a intraplate samples have undergone high-pressure and/or polybaric fractional crystallization. Annotated cotectic curves are from Sack *et al.* (1987) and references therein. The old and young series apparently have primary differences in their degree of silica saturation, shown by their different calculated normative nepheline proportions. However, crustal contamination would drive compositions away from the nepheline apex, and could, in part, be responsible for the less silica-undersaturated nature of the older series.

Pb and high $^{87}Sr/^{86}Sr$ and low $^{143}Nd/^{144}Nd$ ratios have higher LILE/HFSE and LILE/LREE ratios than other samples (e.g. Ba/Nb; Fig. 10a), although ratios such as Nb/La (1·43–0·90) and Ba/Nb (7–14) are within the range of oceanic basalts (Weaver, 1991). Compared with mafic samples whose multielement patterns peak at Nb (Fig. 5), evolved samples with enriched isotopic compositions peak at Ba, and the patterns of the evolved samples amongst the VICE are also typically more spiky than that of the primitive samples. Similarly, small positive Pb anomalies characterize the more evolved and isotopically enriched samples.

The range in isotopic composition and incompatible trace element ratios exhibited by the Sana'a samples is no larger than that observed in many individual ocean islands, and is considerably less than that inferred for all asthenosphere- or plume-derived oceanic basalts (Zindler & Hart, 1986; Weaver, 1991). However, the Sana'a samples were erupted through continental crust, and are clearly not primary magmas. This raises the possibility that crustal contamination produced this isotopic and incompatible trace element heterogeneity rather than melting of heterogeneous lithospheric or asthenospheric mantle sources, or the variable contribution of an enriched LM melt to asthenosphere- or plume-derived magmas.

Isotopic and incompatible trace element variations: mantle heterogeneity or crustal contamination?

The Sana'a intraplate samples exhibit broad correlations between MgO and radiogenic isotope ratios (Fig. 11). Poorer general correlations between silica and isotopic composition are also observed which could, in part, explain the difficulty in producing low residuals for this element when modelling fractional crystallization processes (Baker, 1996). The most evolved sample, trachyandesite JB236, clearly has the most enriched radiogenic isotopic composition. These correlations provide evidence for some crustal contamination of the parental magmas, possibly coupled with fractional crystallization.

Strong support for a crustal contribution to the magmatism comes from isotopic analyses of Pan-African crustal rocks in this region. The Sana'a samples clearly trend towards some published Pan-African crustal components in Pb isotope plots, in particular silicic lower crust of Early Proterozoic–Late Archaean age from Sudan. Moreover, unpublished Pb isotope analyses of gneisses of similar age (1·7–2·3 Ma; Windley *et al.*, 1996) from ~50 km south-east of Sana'a fall close to the intraplate volcanic samples with the most unradiogenic Pb composition (Fig. 7d; J. A. Baker, unpublished data, 1997) and are clearly an appropriate mixing component in Pb isotopic space to generate most of the observed Pb isotopic variation. Such crustal rocks also have Sr–Nd isotopic compositions that could have produced the Sr–Nd isotopic variability observed in the intraplate rocks (Fig. 6b; next section).

The relatively uniform and low $\delta^{18}O$ value of the mantle (Mattey *et al.*, 1994) compared with continental crust should render oxygen an unequivocal indicator of the role of crustal contamination in the petrogenesis of continental basalts. Mantle-derived melts should have

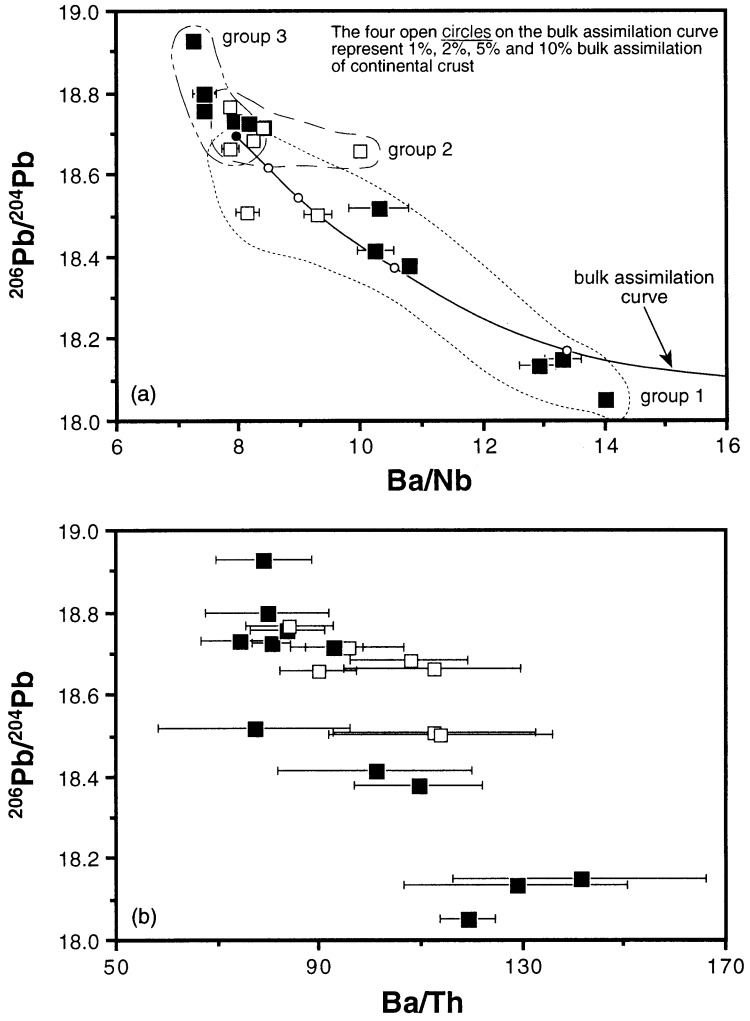

Fig. 10. (a) Ba/Nb vs $^{206}Pb/^{204}Pb$. The continuous line is a bulk assimilation curve for mixing between a hypothetical intraplate basalt with Ba = 320 p.p.m., Nb = 40 p.p.m., Pb = 2 p.p.m. and $^{206}Pb/^{204}Pb = 18{\cdot}7$, and a silicic lower-crustal sample from Davidson & Wilson (1989) with Ba = 2043 p.p.m., Nb = 7 p.p.m., Pb = 14 p.p.m. and $^{206}Pb/^{204}Pb = 17{\cdot}5$. Combined assimilation–fractional crystallization curves do not deviate markedly from bulk assimilation curves at these levels of contamination (<10%). (b) Variation of Ba/Th with $^{206}Pb/^{204}Pb$ ratios.

$\delta^{18}O = 6{\cdot}0$–$6{\cdot}2$‰, and should crystallize olivine phenocrysts with $\delta^{18}O = 5{\cdot}2$‰ at near-liquidus temperatures (1200°C; Mattey *et al.*, 1994; Eiler *et al.*, 1995). Laser fluorination oxygen isotope analyses of olivine phenocrysts from the Sana'a volcanic rocks have a restricted range in composition ($\delta^{18}O = +5{\cdot}2$ to $+5{\cdot}5$‰) and are identical, within assigned analytical uncertainty, to each other and also the heavier part of the $\delta^{18}O$ range defined for mantle olivine by Mattey *et al.* (1994). However, no fresh mineral phase could be separated from the isotopically extreme trachyandesite sample for oxygen isotope analysis. This oxygen isotope homogeneity, at first glance, might appear to provide strong evidence against a crustal contribution to the magmatism. However, this is clearly not the case. Oxygen isotope analyses of Pan-African crust are rare, but Davidson & Wilson (1989) reported five values for Early Proterozoic–Late Archaean crustal samples from Sudan that range from $+8{\cdot}0$ to $+9{\cdot}8$‰, with three silicic lower-crustal samples having lower $\delta^{18}O$ values ($+8{\cdot}0$ to $+8{\cdot}3$‰) within this range. Late Proterozoic crustal rocks from Sinai also have low and often mantle-like oxygen isotope ratios ($\delta^{18}O = +5{\cdot}5$ to $+7{\cdot}0$; Bielski, 1982). Simple bulk mixing and combined assimilation–fractional crystallization calculations (AFC; DePaolo, 1981) between a mantle-derived magma with $\delta^{18}O = 6{\cdot}1$‰ and a hypothetical crustal component with $\delta^{18}O = 8{\cdot}0$‰ can demonstrate that at least 15% of such continental crust can be assimilated without producing a change in $\delta^{18}O$ >0·3‰. However, assimilation of these amounts of crust

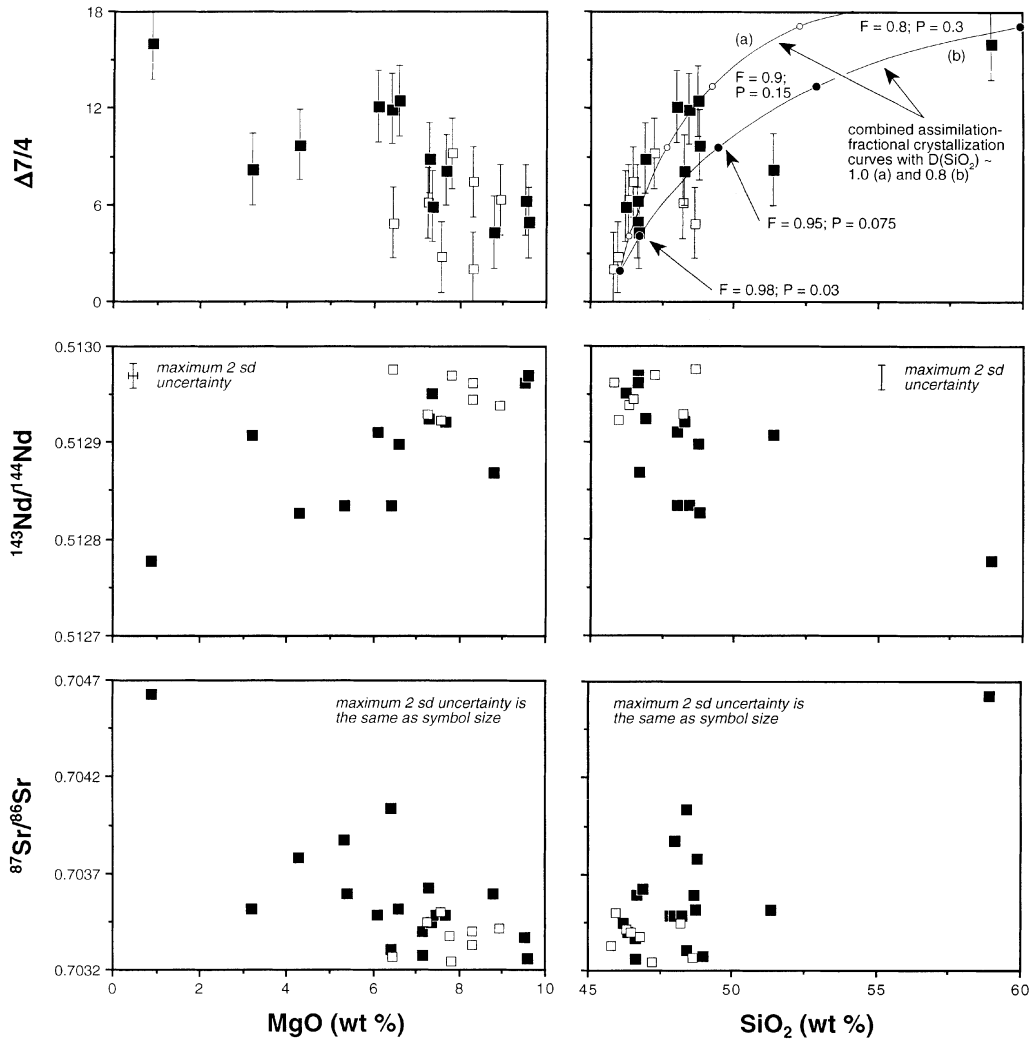

Fig. 11. MgO and SiO_2 vs Δ7/4, $^{143}Nd/^{144}Nd$ and $^{87}Sr/^{86}Sr$. AFC trajectories for the SiO_2–Δ7/4 plot reproduce the hyperbolic arrays exhibited by the Sana'a data and suggest crust/magma ratios of 0–0·2 (*P*; Aitchensen & Forrest, 1994) and the trachyandesite may have *P*~0·25. Parameters used in modelling: rate of assimilation to fractional crystallization (*r*) = 0·6; bulk distribution coefficients: Pb = 0·2; SiO_2 = 1·0 and 0·8; starting magma: SiO_2 = 46 wt %; Δ7/4 = 2; assimilant: SiO_2 = 68 wt %; Δ7/4 = 24. The distribution coefficient for SiO_2 will be close to or slightly less than one during fractional crystallization of ol + cpx + plag, and will be <1 after the onset of Fe–Ti oxide fractionation (MgO <6 wt %). Lower values for *r* will also generate AFC curves that have higher silica contents at a given Δ7/4 than the main trend, and would have lower *F* (fraction of melt remaining) and *P* values than the annotated curves.

will produce marked changes in LILE/HFSE, LILE/LREE, and radiogenic isotope ratios. For example, addition of 15% of a lower-crustal sample (X37: Ba = 2043 p.p.m.; Nb = 7 p.p.m.; La = 62 p.p.m.; Sr = 678 p.p.m.; Pb = 14 p.p.m.; $^{87}Sr/^{86}Sr$ = 0·7086; $^{206}Pb/^{204}Pb$ = 17·6; Davidson & Wilson, 1989) to an intraplate sample (JB253: Ba = 128 p.p.m.; Nb = 12·4 p.p.m.; La = 10 p.p.m.; Sr = 352 p.p.m.; Pb = 0·6 p.p.m.; $^{87}Sr/^{86}Sr$ = 0·70337; $^{206}Pb/^{204}Pb$ = 18·5) produces the following changes in LILE/HFSE, LILE/LREE, and radiogenic isotope ratios: (1) Ba/Nb increases from 10·3 (uncontaminated magma) to 35·8 (contaminated magma); (2) Ba/La increases from 12·8 to 23·4; (3) $^{87}Sr/^{86}Sr$ increases from 0·70337 to 0·7047; (4) $^{206}Pb/^{204}Pb$ decreases from 18·5 to 17·8.

In summary, correlations between MgO and SiO_2 and radiogenic isotopic data, coupled with the clear availability of a crustal component with a suitable Sr–Nd–Pb isotopic composition to generate the trend to enriched isotopic compositions in the intraplate samples, provide strong *prima facie* evidence for crustal contamination playing an important role during magma genesis. The lack of oxygen isotope variability in the intraplate volcanic suite does not, in this case, preclude

crustal contamination during magma ascent through, and storage in, the crust.

Quantitative modelling of crustal contamination processes

The $^{143}Nd/^{144}Nd$ ratio of the crustal contaminant can be gleaned from the linear correlation between Pb/Nd and $^{143}Nd/^{144}Nd$ ratios (Fig. 12a) that can be extrapolated to assumed crustal Pb/Nd ratios (Fig. 12b), and used to estimate a crustal $^{143}Nd/^{144}Nd$ ratio. This yields a value of $^{143}Nd/^{144}Nd$ <0·5120, at realistic levels of contamination (<50%), which is similar to Davidson & Wilson's (1989) Early Proterozoic or Late Archaean crustal samples from Sudan (depleted mantle Nd model ages of 1·9–2·7 Ga) and also the two crustal samples from 50 km south-west of Sana'a. Nd model ages for the Sudanese samples are the same as those for the Abas Gneiss terrane through which the Sana'a magmas were likely to have erupted.

A $^{143}Nd/^{144}Nd$ ratio <0·5120 for the crustal component is clearly much lower than numerous analyses of Late Proterozoic continental crust from Saudi Arabia and is consistent with Pb isotopic systematics (Fig. 7d) which require an Early Proterozoic or Late Archaean crustal contaminant. Isotopically extreme and enriched LM xenoliths from Tanzania (Cohen *et al.*, 1984) have Pb/Nd ratios much too low to generate the observed Pb/Nd–$^{143}Nd/^{144}Nd$ co-variation (Fig. 12b).

Hypothetical bulk mixing and AFC trajectories in Sr–Nd isotopic space that model crustal contamination of an average mafic Sana'a basalt are illustrated in Fig. 13. These calculations indicate that:

(1) 0–20% assimilation of a crustal component with $^{87}Sr/^{86}Sr$ ~0·7100 and $^{143}Nd/^{144}Nd$ ~0·5115 and realistic Sr and Nd concentrations for continental crust could account for all the observed Sr–Nd isotopic variation in the Sana'a volcanic rocks;

(2) younger Late Proterozoic crust with higher $^{143}Nd/^{144}Nd$ ratios would require unrealistically large amounts of contamination (>40–50%) to generate the observed range of $^{143}Nd/^{144}Nd$ ratios;

(3) the scatter in the Sr–Nd isotopic array is probably a function of: (a) crustal isotopic heterogeneity; (b) variations in the bulk distribution coefficient for Sr during the fractionation–contamination sequence, but only if the rate of fractional crystallization to assimilation was variable and, in particular, lower during generation of the samples that fall to the right of the Sr–Nd isotopic array; or (c) variations in the concentration ratios of Sr and Nd in the crustal and magma end-members.

Bulk mixing calculations between an intraplate basalt and a silicic lower-crustal sample from Sudan are also able to reproduce the Ba/Nb–$^{206}Pb/^{204}Pb$ correlation illustrated in Fig. 10a (combined AFC trajectories for the Ba/Nb vs $^{206}Pb/^{204}Pb$ plot do not deviate markedly from the bulk mixing curve). A similar correlation between Ba/Th and $^{206}Pb/^{204}Pb$ ratios (Fig. 10b) cannot be explained by assimilation of upper continental crust which has Ba/Th ~67 (Taylor & McLennan, 1985), and is again consistent with assimilation of lower crust similar to the Early Proterozoic or Late Archaean crustal samples from Sudan, some of which have high Ba/Th ratios (40–220).

Interestingly, Pb isotopic variations in the Sana'a samples coupled with modelling of the Sr–Nd isotopic variations yield good constraints on the nature of the continental crust underlying the Sana'a volcanic field. The conclusion that a relatively old, Early Proterozoic or Late Archaean, crustal component underlies this region is in accord with recent isotopic studies of continental crust in Yemen (Windley *et al.*, 1996) and illustrates the potential of using such volcanic rocks as probes of the continental crust they have traversed rather than, as is frequently invoked, as probes of the LM.

In summary, variations of some VICE and Sr–Nd–Pb–O isotope ratios are consistent with assimilation of 0–20% crustal material. The crustal component clearly has Sr–Nd–Pb isotopic ratios appropriate for Pan-African crust, and this is probably Early Proterozoic to Late Archaean silicic lower crust.

Quantification of the amounts of crustal contamination beyond the approximations given in this section is impossible given the uncertainties regarding: (1) primary melt incompatible trace element concentrations, which are clearly variable, and unrelated to isotopic composition; (2) the chemical and isotopic composition of the assimilant—even Pan-African crust of restricted age and type is extremely heterogeneous, e.g. silicic lower crust from Sudan—$^{87}Sr/^{86}Sr = 0·709–0·730$; $^{143}Nd/^{144}Nd = 0·5107–0·5114$ (Davidson & Wilson, 1989); (3) uncertainties in the contamination calculations, e.g. variable rates of assimilation to fractional crystallization (r), and variable bulk distribution coefficients for Sr during assimilation and fractional crystallization. It is these factors that are likely to be responsible for the rather scattered trends observed in Figs 6–13.

Although other examples of Arabian intraplate volcanic rocks have a more restricted range in isotopic composition than the Sana'a samples, this should not necessarily be taken as evidence against them having undergone substantial contamination. Much of the intraplate volcanism in Israel, Saudi Arabia and Jordan was probably erupted through Neoproterozoic juvenile Pan-African crust. Such crust is isotopically less extreme than that through which the Sana'a volcanic rocks were erupted, and would be unable to generate isotopic variations of the same magnitude as that in Yemen at broadly similar levels of contamination.

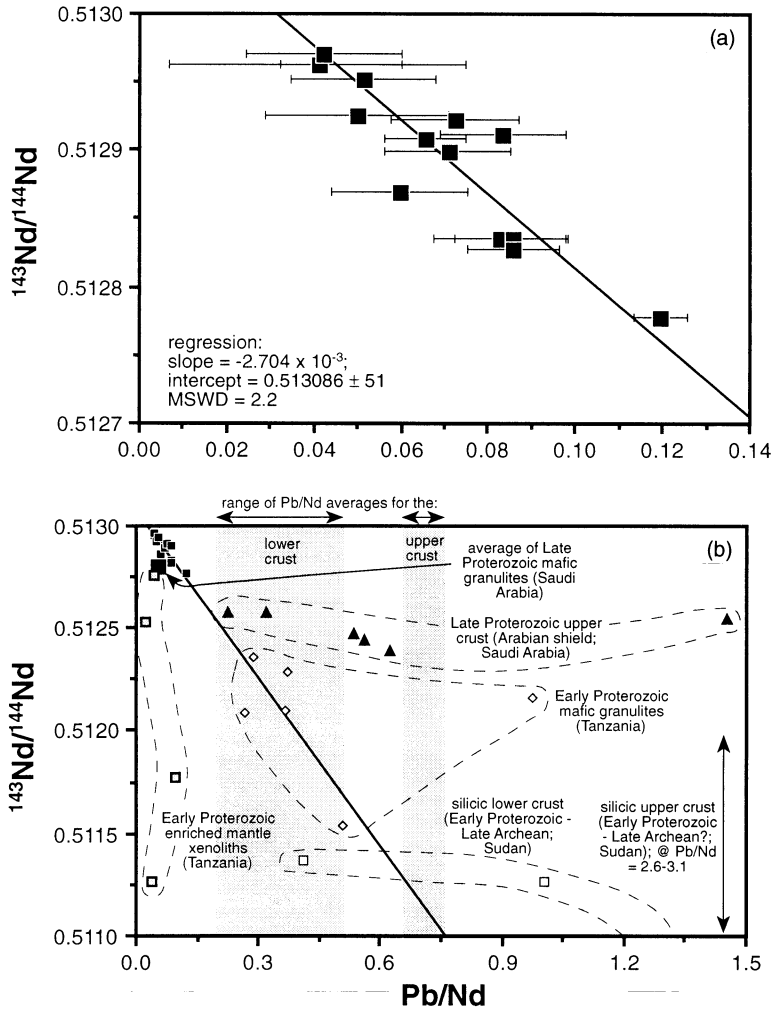

Fig. 12. (a) Correlation between Pb/Nd and $^{143}Nd/^{144}Nd$ ratios defined by the old series volcanic rocks (the young series have lower Pb contents which leads to large uncertainties in Pb/Nd ratios and as such are not included in this figure). (b) The linear correlation is consistent with mixing between mantle-derived magmas and crustal rocks, rather than mixing with an enriched LM component as defined, for example, by the Tanzanian mantle xenolith data. Bulk mixing calculations using appropriate samples from close to the mixing line in the three crustal fields would require addition of $\gg$30% Late Proterozoic Saudi Arabian crust, 10–12% Early Proterozoic–Late Archaean Sudanese silicic lower crust, or 60–70% Early Proterozoic–Late Archaean Tanzanian mafic granulites to generate the range of Pb/Nd and $^{143}Nd/^{144}Nd$ ratios exhibited by the intraplate volcanic rocks. Models invoking contamination by Early Proterozoic–Late Archaean Sudanese silicic lower crust are also consistent with the Pb isotopic composition of the assimilant (Fig. 7d). The sources of comparative data are the same as in Figs 6 and 7. Average upper-crustal compositions are from Taylor & McLennan (1985), Shaw *et al.* (1986) and Condie (1993). Average lower-crustal compositions are from Weaver & Tarney (1984), Taylor & McLennan (1985) and Rudnick & Taylor (1987).

The primary isotopic and trace element signature of the Sana'a magmas

The least contaminated samples have isotopic compositions that are within the following approximate range: $^{87}Sr/^{86}Sr = 0{\cdot}70325$–$0{\cdot}70350$; $^{143}Nd/^{144}Nd = 0{\cdot}51297$–$0{\cdot}51290$; $^{206}Pb/^{204}Pb = 18{\cdot}65$–$18{\cdot}95$; $\Delta 7/4 = +2$; $\Delta 8/4 = +35$. The exact primary isotopic composition before crustal contamination, or whether a range of compositions existed, is difficult to resolve, but there is likely to have been some mantle isotopic heterogeneity within the above ranges; however, we stress that most of the range in isotopic composition (65–80%) exhibited by the intraplate rocks, and nearly all of the range of LILE/HFSE ratios, is the result of crustal contamination.

The primary incompatible trace element compositions of the most primitive magmas are characterized by low ratios of LILE/HFSE compared with MORB (e.g. K/Nb $\leq$200 vs K/Nb ~290 in MORB; Weaver, 1991), which are manifest as negative-K anomalies on multi-element diagrams. K/Nb ratios are not, however, as low as for Djiboutian intraplate magmas produced from the Afar plume (K/Nb <150; Deniel *et al.*, 1994) and

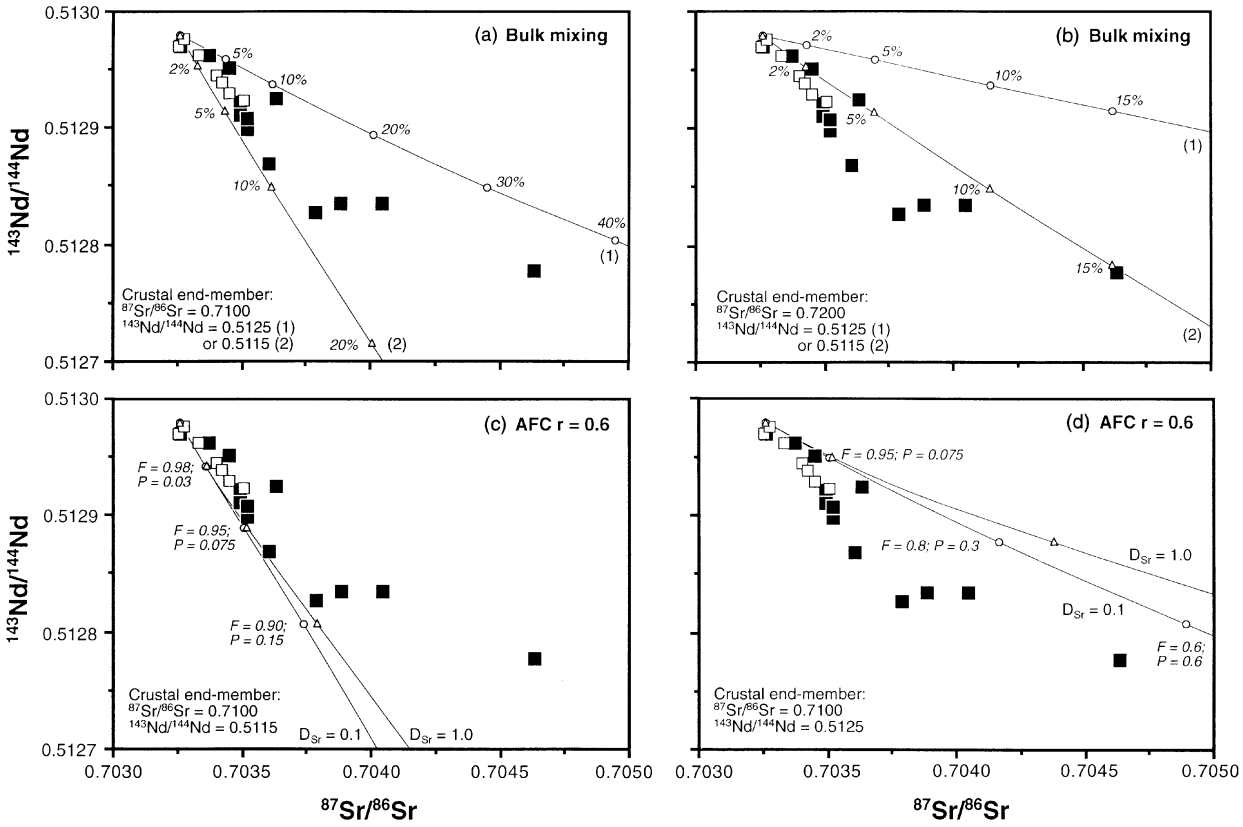

Fig. 13. (a) and (b), bulk mixing calculations illustrating the possible effects of bulk assimilation of continental crust by the Sana'a volcanic rocks. The uncontaminated basalt composition used in modelling has $^{87}Sr/^{86}Sr = 0{\cdot}70326$, $^{143}Nd/^{144}Nd = 0{\cdot}51298$, Sr = 600 p.p.m. and Nd = 30 p.p.m. The crustal component used in the modelling has Sr = 300 p.p.m. and Nd = 26 p.p.m. (Taylor & McLennan, 1985; average from Davidson & Wilson, 1989); the isotopic composition of the assimilant is annotated on the graphs. (c) and (d), combined assimilation–fractional crystallization (AFC; DePaolo, 1981) calculations illustrating the possible effects of assimilation of continental crust by the Sana'a intraplate volcanic rocks. The uncontaminated basalt and crustal compositions used in modelling are the same as in (a) and (b). Two curves are calculated for each diagram with bulk distribution coefficients for Sr of 0·1 and 1·0. The bulk distribution coefficient for Nd was taken as 0·1. *F*, fraction of melt remaining; *P*, proportion of crust to magma (Aitchensen & Forrest, 1994).

Oligocene flood basalts also derived from this plume (K/Nb <150; Baker *et al.*, 1996). PM-normalized multi-element patterns peak at Nb and are OIB-like. Given the high LILE/HFSE ratios of continental crust, the very low LILE/HFSE ratios of the Sana'a rocks, and the highly susceptible nature of such ratios to contamination, the least contaminated samples must have primary isotopic compositions that are close to those defined above.

The primary isotopic signature of the Sana'a magmas is intermediate between Gulf of Aden–Red Sea MORB and the Afar plume composition, although this signature is closer to the plume composition, and is also almost identical to analyses of Ataq LM xenoliths (Figs 6 and 7) and, in some respects, similar to some intraplate basalts from Saudi Arabia (Altherr *et al.*, 1990). However, in detail, Arabian intraplate basalts (Figs 6, 7 and 9), and also those from Sinai and Israel (Stein & Hofmann, 1992), are characterized by lower $^{87}Sr/^{86}Sr$ ratios and lower $\Delta 7/4$ and $\Delta 8/4$ values than the Sana'a samples.

Partial melting

Qualitative observations

Ratios of VICE/MICE such as Ce/Y (0·85–3·70) and Nb/Zr (0·078–0·313) vary widely in the Sana'a samples. Those with higher VICE/MICE ratios are typically more silica undersaturated and alkaline. Increasing Zr/Nb ratios are accompanied by decreasing Ce/Y ratios, although there is some scatter associated with this trend (Fig. 14). This general correlation cannot be the product of the following processes.

Fractional crystallization. Zr/Nb and Ce/Y ratios do not correlate with MgO content and, in any case, fractional

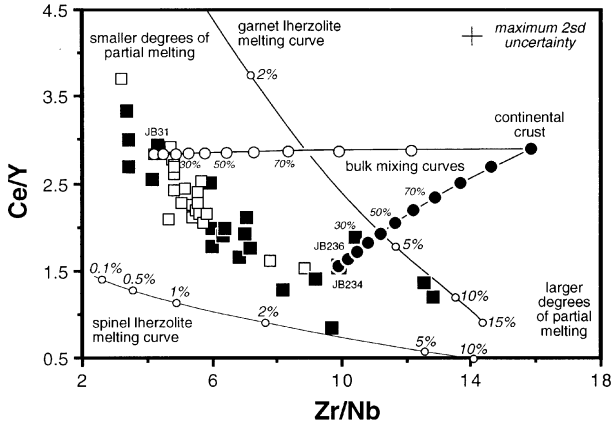

Fig. 14. Variation of Zr/Nb vs Ce/Y for the Sana'a samples. Crustal contamination curves were calculated assuming bulk mixing, two samples from either end of the Zr/Nb vs Ce/Y data array, and an upper-crustal estimate from Taylor & McLennan (1985), but using a different Nb value for the crust based on Zr/Nb ratios of other studies (Shaw *et al.*, 1986; Davidson & Wilson, 1989; Condie, 1993). Representative point-average, non-modal, fractional melting curves are plotted on each diagram for spinel and garnet lherzolite sources, using a primitive mantle bulk composition. Maximum 2 SD uncertainties for Zr/Nb and Ce/Y are shown, although these are almost always smaller than the symbol size.

crystallization of predominantly ol + cpx + plag can only generate small changes in these ratios, e.g. cpx is the phase most effective in fractionating Zr/Nb ratios given D_{Zr}/D_{Nb} ~3–20 (M. F. Thirlwall, unpublished data, 1995), yet even 50% fractionation of cpx from an intra-plate magma with Zr/Nb = 10 would only lower Zr/Nb to 9·1.

Crustal contamination. Continental crust is generally characterized by Zr/Nb >10 and high Ce/Y ratios (e.g. Taylor & McLennan, 1985). Contamination of any sample in Fig. 14 would not produce the observed data array. Moreover, VICE/MICE ratios are not correlated with isotopic composition. Simple mixing calculations indicate that addition of continental crust will only produce small changes in Zr/Nb and Ce/Y ratios and this change will be roughly perpendicular to the main trend in Fig. 14. The most contaminated trachyandesite sample, JB236, is actually displaced in this fashion away from the main array of data.

Long-lived mantle heterogeneity. The large range in Ce/Y ratios is coupled with a substantial range in Sm/Nd ratios (0·178–0·233). This variation cannot be attributed to mantle source heterogeneity unless such enrichment was recent (<100–200 m.y.); older enrichment events would permit greater development of Nd isotopic heterogeneity (>0·00005 in 100–200 m.y.) and, furthermore, there is no correlation between Sm/Nd and $^{143}Nd/^{144}Nd$ ratios in these rocks. A wide range in U/Pb ratios in samples with a restricted range in, for example, Δ7/4 values places even tighter constraints on any possible mantle enrichment event. $^{238}U/^{204}Pb$ values of samples that have not been significantly crustally contaminated vary from 20 to 61 and would produce variations in $^{206}Pb/^{204}Pb$ >0·5, with essentially constant $^{207}Pb/^{204}Pb$ values, in 80 m.y.

Variable degree of partial melting is thus clearly the simplest explanation to account for the variation in VICE/MICE ratios that are not associated with isotopic variability, with samples representing smaller melt fractions having higher VICE abundances and VICE/MICE ratios.

Semi-quantitative melt modelling

The melt models presented in Figs 14–16 use point-average, non-modal, fractional melt modelling (Shaw, 1970) to test the hypothesis that the Sana'a volcanic rocks were produced by variable degrees of partial melting. Rigorous quantification of the melting process is not possible as the composition of the mantle source is difficult to constrain. However, modelling of the REE and Nb, Zr and Y data can place some powerful constraints on the origin of the trace element heterogeneity observed in these rocks.

Modelling used the REE distribution coefficient compilation of McKenzie & O'Nions (1991), with distribution coefficients for Y assumed to be the same as for Ho, and distribution coefficients for Zr and Nb calculated from phenocryst–host volcanic rock data (M. F. Thirlwall, unpublished data, 1995). The Zr and Nb distribution coefficients were adjusted so that the distribution coefficients for La (Nb) and Sm (Zr) from the studies by Thirlwall and McKenzie & O'Nions were made comparable, i.e. $D_{Zr,Nb}$(Thirlwall) values were multiplied by $D_{Sm,La}$(McKenzie & O'Nions)/$D_{Sm,La}$(Thirlwall). Source compositions for depleted MORB mantle (DMM) are from McKenzie & O'Nions (1991) and Kostopoulos

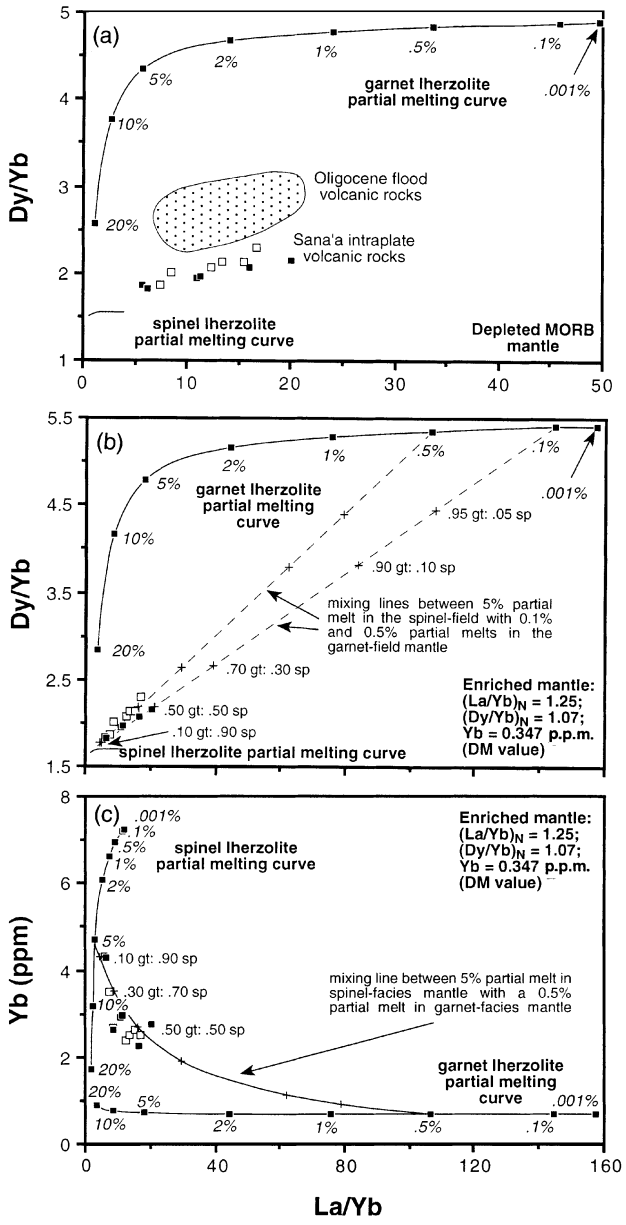

Fig. 15. La/Yb vs Dy/Yb and Yb. Melt curves are point-average, non-modal, fractional melts of garnet and spinel lherzolites (garnet lherzolite: 0·598 ol, 0·211 opx; 0·076 cpx, 0·115 gt that melts in the proportions 0·05 ol, 0·20 opx, 0·30 cpx, 0·45 gt; spinel lherzolite: 0·578 ol, 0·270 opx, 0·119 cpx, 0·033 sp that melts in the proportions 0·10 ol, 0·27 opx, 0·50 cpx, 0·13 sp; Thirlwall *et al.*, 1994). Curves are also shown that represent mixing between small melt fractions from the garnet-facies mantle and somewhat larger melt fractions from spinel-facies mantle. Distribution coefficients were taken from McKenzie & O'Nions (1991).

& James (1992); primitive mantle (PM) values are from Taylor & McLennan (1985).

Fractional melting curves for a garnet and spinel lherzolite with a PM composition are shown on a plot of Zr/Nb vs Ce/Y in Fig. 14. The observed array of data is not closely modelled by variable degrees of melting of PM in either the spinel or garnet facies. Using a more enriched source composition can generate a garnet-facies mantle melting curve closer to the observed data in Fig. 14. An important point from modelling Zr/Nb and

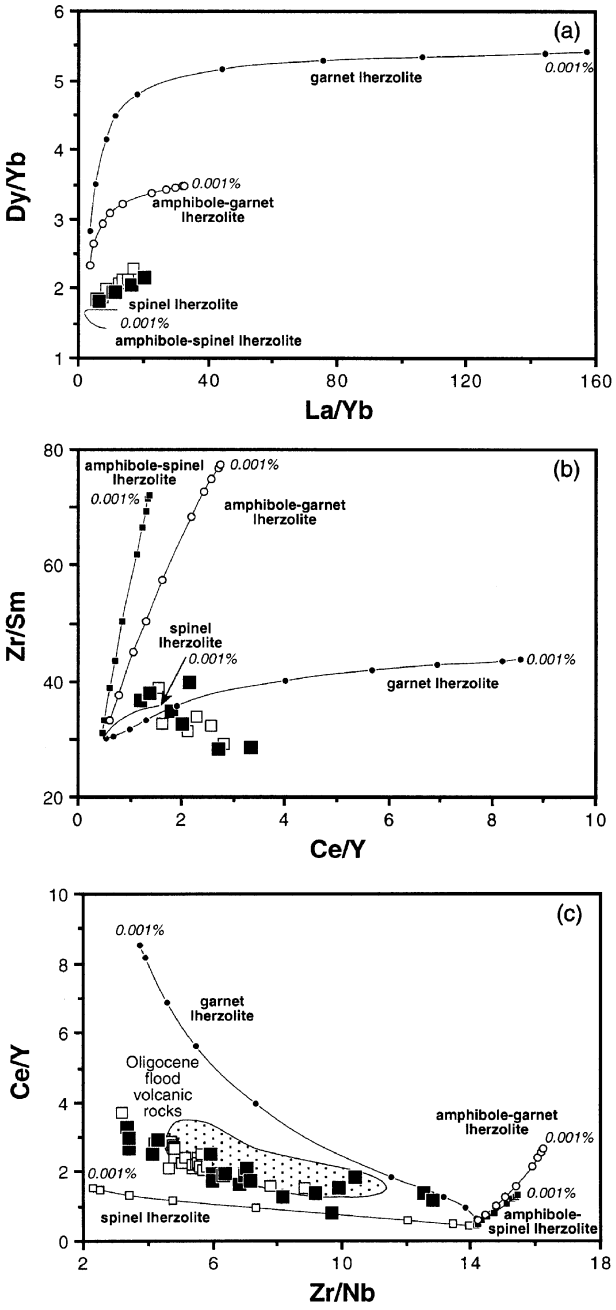

Fig. 16. Variation of La/Yb vs Dy/Yb, Zr/Sm and Ce/Y for the Sana'a volcanic rocks. Point-average, non-modal, fractional melting curves for amphibole-bearing spinel and garnet lherzolites are plotted as continuous curves. The source composition used in modelling is the same as that in Fig. 15, as are the modal mineralogy and melting proportions of the spinel and garnet lherzolites. The amphibole-bearing sources are: (a) amphibole–garnet lherzolite: 0·55 ol, 0·19 opx, 0·07 cpx, 0·08 gt, 0·11 amph that melts in the proportions 0·05 ol, 0·15 opx, 0·25 cpx, 0·3 gt, 0·25 amph; (b) amphibole–spinel lherzolite: 0·554 ol, 0·250 opx, 0·080 cpx, 0·033 sp, 0·083 amph that melts in the proportions 0·08 ol, 0·25 opx, 0·27 cpx, 0·13 sp, 0·27 amph. The melting curves are not greatly affected by changes in these parameters and they are simply chosen so that the critical phases (garnet, clinopyroxene and amphibole) do not become exhausted during melting. Each of the melting curves, where large enough, is annotated with points that represent the following degrees of melting: 0·001%, 0·1%, 0·5%, 1%, 2%, 5%, 7·5%, 10%, 15% and 20%. The small-degree partial melt end of the curve is marked in each plot.

Ce/Y ratios is that a DMM source cannot produce the low Zr/Nb ratios observed in these rocks, even at the smallest degrees of partial melting (not shown).

A more useful approach to melt modelling is the use of plots of LREE/HREE vs MREE/HREE ratios, e.g. La/Yb vs Dy/Yb. These plots are particularly useful as they distinguish between melting in the spinel and garnet stability fields (Thirlwall *et al.*, 1994; Baker *et al.*, in preparation). Spinel-facies melting produces little change in Dy/Yb ratios in melts compared with their mantle source and there is also little change in Dy/Yb with melt fraction—monitored by La/Yb ratios (Fig. 15). In contrast, garnet-facies melting produces large changes in Dy/Yb ratios with melt fraction, and the melt ratio is very different from the source ratio. A second feature of such plots is that mixing between different melt fractions will generate linear mixing arrays.

Modelling of La/Yb and Dy/Yb ratios, coupled with Yb abundances, is presented in Fig. 15. The following points can be gleaned from these models:

(1) Variable degrees of partial melting of a spinel lherzolite cannot generate the observed co-variation in Dy/Yb ratio with changing La/Yb ratio (Fig. 15a and b). Melting of a spinel lherzolite should also produce a steep positive correlation between La/Yb ratios and Yb abundances (Fig. 15c). Although Yb abundances in the Sana'a samples are partly controlled by fractional crystallization, it is clear from Fig. 15c that Yb varies by a factor of two, even in samples with <2 wt % range in MgO. Generating these variations in Yb would require fractional crystallization of >50%. Moreover, samples with almost identical MgO contents have very different Yb abundances (e.g. JB233: MgO = 8·8 wt %, La/Yb = 16·0 and Yb = 2·27 p.p.m.; JB252: MgO = 8·9 wt %, La/Yb = 8·31 and Yb = 2·71 p.p.m.). In light of this, there appears to be a negative correlation between La/Yb ratios and Yb abundances, which is a primary feature of the Sana'a samples, and is again inconsistent with variable degrees of melting of a spinel lherzolite. Although partial melting of a harzburgite could generate a positive La/Yb vs Dy/Yb correlation (not shown), it would also be unable to account for the negative correlation between La/Yb ratios and Yb abundances.

(2) Variable degrees of partial melting of a garnet lherzolite cannot generate the La/Yb–Dy/Yb systematics of the Sana'a samples. First, melting a garnet lherzolite with a typical mantle composition (i.e. chondrite-normalized Dy/Yb~1) produces melts with much higher Dy/Yb ratios than the Sana'a samples at reasonable degrees of melting (<20%; Fig. 15a and b)—the mantle source would require an unusually low Dy/Yb ratio if the samples were to be simply the product of garnet lherzolite melting, even if the garnet/cpx of the source was decreased from those used in the models. Second, melting a garnet-facies lherzolite should produce partial melts exhibiting no co-variation between La/Yb ratios and Yb abundances, as Yb is essentially retained or buffered by garnet in the source (Fig. 15c).

(3) The simplest model to account for the REE systematics of the Sana'a samples involves mixing of small melt fractions from garnet-facies mantle with relatively larger melt fractions from spinel-facies mantle (Fig. 15b). Such a model can qualitatively account for the following features of their geochemistry: (a) the near-linear La/Yb vs Dy/Yb correlation at Dy/Yb ratios intermediate between those produced by melting garnet- and spinel-facies mantle with Dy/Yb ratios typical of the upper mantle, i.e. a relatively flat chondrite-normalized MREE–HREE profile; (b) the negative correlation between La/Yb ratios and Yb abundances (Fig. 15c); (c) the hyperbolic array of data in the Zr/Nb vs Ce/Y plot (Fig. 14; given that $[Nb/Y]_{gt\text{-}facies\ melt}/[Nb/Y]_{sp\text{-}facies\ melt} \gg 1$), which is intermediate between spinel- and garnet-facies lherzolite melting curves.

Further development of the model outlined above requires an assessment of the likely mantle source composition. The minimum melt Dy/Yb ratio, 1·71 (chondrite-normalized Dy/Yb = 1·10), can be obtained by extrapolating a regression through the intraplate data to La/Yb = 0 (not shown). As fractional melting in the spinel field only generates an ~2·6% increase in Dy/Yb, the minimum (spinel-) source Dy/Yb value is 1·67 (chondrite-normalized Dy/Yb = 1·07). This is essentially a nearly flat, or slightly MREE-enriched MREE–HREE profile. It is more difficult to estimate the profile of the REE pattern in the LREE–MREE region. The $^{143}Nd/^{144}Nd$ ratios of the least contaminated samples (~0·51297–0·51290) suggest some long-term LREE depletion relative to chondritic mantle sources, although not as extreme as the DMM source. To generate a garnet-facies melt curve that will be intersected by a regression through the Sana'a data, either the source must have a significantly less depleted LREE profile than DMM, or the garnet/clinopyroxene ratio of the source must be increased dramatically. Both will stretch the garnet-facies melt curve parallel to the La/Yb axis. However, increasing the garnet/clinopyroxene ratio of a near-DMM source results in much larger fractionation of the REE relative to Zr/Nb and it is no longer possible to produce the low Zr/Nb ratios required of the garnet-facies melt component. Similarly, the DMM source cannot produce the low Zr/Nb ratios and high LREE concentrations of the intraplate volcanic rocks (not shown).

Clearly, the most appropriate solution is to invoke a more enriched source than DMM, although it is impossible to assess the precise composition of this source. Figure 15b illustrates melting curves for a hypothetical slightly LREE-enriched source with chondrite-normalized La/Yb = 1·25 and Dy/Yb = 1·07, which is a log–linear chondrite-normalized REE profile, and has a

Yb concentration equal to that of DMM. Higher Yb concentrations, for example PM values, in the source generate concentrations of HREE in the melts that are too high compared with the Sana'a volcanic rocks.

Although this model is only semi-quantitative, and partly dependent on the nature of the chosen mantle source, the following conclusions can be drawn from this REE modelling:

(1) Mixing of small degree melts (<1%) and larger degree melts (~5%) from garnet- (deep) and spinel-facies (shallow) mantle, respectively, can account for the observed REE data. The degree of melting inferred for the garnet-facies mantle is strongly dependent on the assumed source composition and modal mineralogy, i.e. garnet/clinopyroxene ratio of the source.

(2) Melting of an LREE-depleted mantle source is permitted in the spinel field as it merely results in translation of the spinel melt curve to lower La/Yb ratios, but a relatively enriched source with respect to a DMM source is required in the garnet-facies mantle. In fact, the mantle source needs to have chondrite-normalized La/Yb ≥ 1, for a regression through the Sana'a data to intersect a garnet-facies melting curve. As the Nd isotopic composition of least contaminated intraplate basalts ($\varepsilon_{Nd} > +5$) implies long-term LREE depletion, it seems probable that the mantle source has experienced recent enrichment in incompatible trace elements.

(3) Melt fractions in the garnet field are fractions of a percent whereas those in the spinel field are probably several percent ($\geq 5\%$). Fluctuations in the degree of partial melting in the spinel field are difficult to monitor given the small range in La/Yb ratios generated by spinel-facies melting, and the non-primary nature of the Sana'a basalts prevents rigorous use of HREE abundances to monitor changes in the degree of spinel-facies melting (e.g. La/Yb vs Yb plot; Fig. 15c). Some scatter in the La/Yb vs Dy/Yb array (Fig. 15b) might be accounted for by small fluctuations in the degree of melting of garnet-facies mantle. However, crustal contamination and extensive fractional crystallization may also be able to generate some of this scatter, and given the large distance over which it is necessary to extrapolate a regression through the volcanic data to intersect the garnet-facies melt curve it is impossible to be confident that there was no variation in the degree of melting in the garnet-facies mantle. The old series sample with the highest La/Yb ratio (JB210), which is largely responsible for the apparently diverging array of the old and young sample groups is, in fact, rather evolved (MgO = 4·3 wt %) and is the most contaminated intraplate sample for which REE data are available ($^{143}Nd/^{144}Nd = 0{\cdot}51283$).

(4) The proportion of melt derived from spinel- and garnet-facies mantle is not highly dependent on the composition of the mantle chosen for each facies (except the Dy/Yb ratio of the source, which is relatively tightly constrained). The simple model presented here suggests that individual samples comprise 40–90% melt derived from spinel-facies mantle (Fig. 15b). Using these figures it can be calculated that between 33 and 83% of the Nd in the intraplate rocks comes from spinel-facies mantle. This relatively large range, coupled with the lack of a correlation between Dy/Yb and $^{143}Nd/^{144}Nd$ ratios, implies that the garnet- and spinel-facies mantle sources were chemically and isotopically heterogeneous.

(5) The young series from the Sana'a suite is offset to slightly lower La/Yb at the same Dy/Yb ratios compared with the old series. This could reflect generation of the younger samples by larger degrees of melting in the garnet-facies mantle, or derivation of garnet-facies melts from a source with a slightly more depleted composition and/or a lower garnet/clinopyroxene ratio than the older samples. However, as already stated in (3), it is not possible to be confident that the two sample groups really form different arrays. In any case, one of the most striking features of the Quaternary intraplate basalts is the apparently higher abundances of VICE and VICE/MICE ratios in the young series compared with the old series subset. This difference is contrary to what would be predicted if the younger samples comprised larger melt fractions in their garnet-facies component. The solution to this problem is not obvious from Fig. 15, as it seems here as if the old and young series have a similar range in La/Yb and Dy/Yb ratios, and hence contain similar proportions of garnet- and spinel-facies melts. This is purely a function of sample selection; Ce/Y ratios correlate perfectly with La/Yb ratios and it is obvious from Fig. 14 that only six of the old series have Ce/Y, and hence La/Yb, ratios greater than the bulk of the young series. Thus, the general incompatible trace element differences between the old and young series reflect generally larger proportions of garnet-facies, or deeper melts, in the young series.

Finally, it is interesting to note two further features of the incompatible trace element data that further complicate the partial melting scenario described above. The first concerns the substantial co-variation between Zr/Sm and VICE/MICE ratios observed in the samples (Fig. 16). The Zr/Sm ratio is usually rather constant in most mantle-derived magmas and inferred source regions, e.g. estimates for DMM, PM and chondrite range from 25 to 34 (Taylor & McLennan, 1985; Sun & McDonough, 1989); 29 Oligocene flood basalts from Yemen have Zr/Sm = 30·1 ± 2·8 (2 SD; Baker, 1996). This is because of the similar incompatibility of Zr and Sm in most igneous systems. The Zr/Sm ratio is not sensitive to the effects of crustal contamination or fractional crystallization, unless amphibole is a fractionating phase. For example, fractional crystallization of 50% clinopyroxene would only increase the Zr/Sm ratio of a residual magma by 5% (based on distribution coefficients from McKenzie &

O'Nions, 1991; M. F. Thirlwall, unpublished data, 1995). Similarly, 20% bulk crustal contamination of an intraplate basalt by a crustal component only produces changes in Zr/Sm of <10%. In normal four-phase spinel or garnet lherzolites, incompatibility of Zr is similar to, or slightly more than, that of Sm, and Zr/Sm will be constant, or positively correlate with VICE/MICE ratios such as Ce/Y as a result of variable degrees of partial melting (Fig. 16). In fact, the Sana'a intraplate volcanic rocks define exactly the opposite relationship, and Zr/Sm varies from 40 to 28 with increasing Ce/Y ratios (Fig. 16). Mixing between melts from anhydrous spinel and garnet lherzolites is unable to produce the marked negative correlation between Zr/Sm and VICE/MICE ratios.

Simply melting an amphibole-bearing spinel or garnet lherzolite also cannot generate the observed trends, as this produces: (1) a negative correlation between La/Yb and Dy/Yb ratios in the case of a spinel lherzolite; (2) positive correlations between Ce/Y and Zr/Sm ratios and a negative or no correlation between Zr/Nb and Zr/Sm ratios; (3) higher Zr/Nb than the source or very little fractionation of Zr/Nb with changing Ce/Y (melt fraction). However, mixing between melts from an amphibole-bearing spinel lherzolite with small degree partial melts from an anhydrous garnet lherzolite might be able to produce a marked negative correlation between Ce/Y and Zr/Sm ratios. The garnet source cannot contain residual amphibole, as this prevents formation of low Zr/Nb melts (Fig. 16c). The absence of amphibole in the garnet lherzolite may be consistent with phase relationships that indicate amphibole is stable only in the spinel stability field and at the very top of the garnet stability field (P <32 kbar—Olafsson & Eggler, 1983; Wallace & Green, 1988).

However, Fig. 16b indicates that the Zr/Sm ratio of the mantle sources must be considerably lower (<20) than the value of 30 assumed for the source in the models presented here. Alternatively, it might be possible that a residual Zr-bearing phase, which was not exhausted at the small degrees of melting which characterized garnet-facies mantle, could have produced the low Zr/Sm ratio of the garnet-facies melts (this would produce a negative Ce/Y vs Zr/Sm correlation). However, this in itself would not be sufficient to account for the Ce/Y vs Zr/Sm relationships unless amphibole is present in the spinel-facies source, as the data do not project into an appropriate part of the anhydrous spinel-facies melting curve (i.e. at melt fractions >1%). Moreover, the presence of a residual Zr-bearing phase seems unlikely, as ratios of VICE/Zr exhibit the same magnitude of variation as most other VICE/MICE ratios.

Mixing between melts from an amphibole-bearing spinel lherzolite and an anhydrous spinel lherzolite is also unable to reproduce the observed data in Figs 13–16, unless the anhydrous lherzolite is significantly more enriched in incompatible trace elements. This seems to be the opposite to what would be expected, with the presence of amphibole likely to have been coupled with incompatible trace element enrichment.

The second line of evidence supporting the presence of amphibole in the spinel-facies source comes from examination of Nb/La ratios. Although Nb/La ratios are to some extent affected by crustal contamination, samples with $^{143}Nd/^{144}Nd > 0{\cdot}51285$ have Nb/La = 0·90–1·43. Yet 10% of bulk crustal contamination would only lower the Nb/La ratio of a sample with Nb/La = 1·4 by 0·1. We suggest that some of the variation in Nb/La ratios is a function of the presence of amphibole in the spinel-facies mantle. Unfortunately, crustal contamination does preclude the use of the Nb/La ratio in modelling this hypothesis, and also definitely rules out the use of LILE in evaluating the possible role of amphibole in the mantle source region.

Comparison with Oligocene flood volcanism

The Sana'a intraplate samples all have Dy/Yb ratios significantly lower than those of Oligocene flood basalts in western Yemen (Baker, 1996; Fig. 15). This difference is readily explained by the flood basalts containing a greater proportion of garnet-facies melts (90–60%) than the Sana'a samples (60–10%) and being the result of deeper average mantle melting. Clearly, a shallower source for the Sana'a volcanic rocks might be consistent with partial melting of a distinct source from that of the flood basalt volcanism, or ascent of a source similar to that of the flood volcanic rocks to shallower depths, perhaps in response to post-Oligocene lithospheric thinning.

Normal Arabian lithosphere is 100–120 km thick (Mooney *et al.*, 1985). The substantial melt contributions from spinel-facies mantle (<60–80 km) in the Quaternary Sana'a basalts and the Oligocene flood basalts imply that significant lithospheric thinning took place before and during Cenozoic melt generation in Yemen or that the LM was the source of these volcanic rocks.

A final interesting comparison between the Sana'a and flood basalt volcanism relates to the similar Zr/Nb ratios of these suites of rocks (this study and Baker *et al.*, 1996). Intuitively, the Sana'a rocks must represent smaller average degrees of partial melting, yet they have the same Zr/Nb ratios as the flood basalts. This actually requires the Sana'a magmas to be derived from a more depleted source than the flood basalts or, perhaps more realistically, supports the involvement of amphibole as a mineral in the source of the Sana'a rocks, which inhibits Zr/Nb fractionation from source values during melting.

Source and nature of post-flood basalt intraplate volcanism in Yemen

The least contaminated intraplate samples have isotopic and trace element characteristics similar to those of many oceanic basalts. Moreover, this composition approaches that of magmas derived from an Afar plume–MORB mantle mixture and is almost identical to that of recently metasomatized LM xenoliths from Ataq, southern Yemen. We suggest that intraplate volcanism was generated within shallow mantle, either LM or ambient upper mantle allowed to ascend to depths <80 km as a result of Cenozoic lithospheric thinning, that had been recently enriched by predominantly garnet-facies melts with an isotopic composition akin to the Afar plume, which was responsible for Oligocene flood volcanism in Yemen (Baker *et al.*, 1996). Moreover, this enrichment was also accompanied by hydration of the shallow mantle and crystallization of amphibole. Actual examples of such mantle are represented by Ataq LM xenoliths, which contain abundant pargasite–edenite amphibole which give electron microprobe major element totals of ~96–97 wt %, with low halogen contents (Chazot *et al.*, 1996).

Intraplate volcanism is likely to have been the product of melting this shallow enriched and hydrated mantle in response to small amounts of lithospheric extension (e.g. Gallagher & Hawkesworth, 1992) during formation of the Sana'a basin. The fact that the younger suite of intraplate samples contain a larger proportion of melt from garnet-facies mantle is also consistent with a model of melt generation in response to lithospheric extension.

If the mantle beneath Yemen was hydrated during flood basalt volcanism, it has implications for the formation of enriched LM sources and also, perhaps, the mechanics of melt generation in mantle plumes during flood volcanism. Mantle plumes are generally considered to be hotspots whose higher than ambient temperature permits greater than normal amounts of decompression melting. However, if these plumes are also volatile rich they could undergo large amounts of melting without being significantly hotter than ambient upper mantle, and the effects of volatiles fluxing into the lithosphere need to be considered when modelling LM melting.

Implications for Arabian intraplate volcanism

Examples of Late Cretaceous to Recent intraplate volcanism from throughout the Arabian peninsula (Israel, Jordan, Saudi Arabia) are similar, in many respects, to the Yemen example discussed here. In detail, the Sana'a samples have subtly distinct isotopic signatures, in particular higher $\Delta 8/4$ and $^{87}Sr/^{86}Sr$ ratios. This observation seems to preclude models for Arabian intraplate volcanism that invoke channelling of the Afar plume northwards beneath a flexure in the continental lithosphere to beneath Saudi Arabia (Camp & Roobol, 1992). The source of Saudi Arabian intraplate volcanism is more likely to be the result of separate mantle upwellings beneath western Saudi Arabia, or reactivation during Red Sea rifting of shallow LM enriched by earlier mantle plumes, which had a subtly different signature from the Afar plume. We note that shallow mantle enriched by mantle plumes is precisely the source envisaged by Stein & Hofmann (1992) to be the source of Phanerozoic alkali basalts from Israel which have been repeatedly erupted during the last 200 m.y. Volcanism and mantle enrichment in Yemen provides a modern analogue of development of such sources for continental intraplate volcanism.

CONCLUSIONS

A detailed chemical and isotopic study of Quaternary intraplate volcanism in western Yemen, which post-dates a major episode of Oligocene flood basalt volcanism, provides the following constraints on magma genesis:

(1) None of the Sana'a samples represent primary magmas and they have undergone polybaric fractional crystallization of ol + cpx ± plag ± Fe–Ti oxides ± apatite.

(2) Isotopic variation in the samples, although substantially less than that exhibited by oceanic basalts and even individual ocean islands, can be largely explained by assimilation of ~0–20% silicic lower crust of Early Proterozoic to Late Archaean age.

(3) Variations in VICE/MICE ratios, which are unrelated to crustal contamination, are principally the result of the magmas containing variable proportions of melt from deep (garnet-facies; 60–10%) and shallow mantle (spinel-facies; 40–90%). Compared with Oligocene flood basalt volcanism in western Yemen, the Sana'a suite comprises magmas which include greater proportions of melt from shallow (spinel-facies) mantle and thus were generated at shallower average depths than the older flood basalt magmas. Syn- and post-flood-basalt lithospheric thinning as a result of plume erosion at the base of the lithosphere and during rifting of Arabia from Africa can account for the shallower depth of melt generation. The incompatible trace element signature of the Sana'a samples requires a recently enriched mantle source, and variations in Sm/Zr ratios and Nb/La ratios are consistent with the spinel-facies mantle source of the magmas containing amphibole.

(4) The least contaminated isotopic and trace element signature of the Sana'a samples approaches that of the Afar plume or a mixture of the Afar plume and MORB

mantle components. Amphibole-bearing LM xenoliths from Ataq have precisely this signature.

We suggest that the Sana'a volcanism was the result of melting shallow mantle that was hydrated and enriched by the Afar plume during or shortly after the episode of Oligocene flood basalt volcanism. The source may be similar to that represented by the Ataq xenoliths. Partial melting occurred in response to small amounts of recent lithospheric extension. Hydration and enrichment of the shallow mantle by mantle plumes has important implications for the formation of shallow and enriched LM sources of intraplate volcanism, lithospheric growth and models for flood basalt volcanism. The Arabian LM has apparently suffered several episodes of plume-related enrichment events (e.g. Stein & Hofmann, 1992), and we concur with Stein & Hofmann (1994) and Stein & Goldstein (1996) in that mantle plumes, both directly and indirectly, may represent an important mechanism for growth of the continental lithosphere. Finally, it is interesting to speculate that mantle plumes may be 'wet spots' in addition to being 'hot spots', with the volatile flux of mantle plumes having obvious implications for melt generation in flood basalt provinces.

ACKNOWLEDGEMENTS

Mohamed Al-Kadasi and Abdulkarim Al-Subbary are thanked for assistance with fieldwork in Yemen. Gerry Ingram and Giz Marriner assisted with radiogenic isotope determinations and XRF spectrometry, respectively. David Mattey is thanked for allowing access to the stable isotope laboratory at RHUL. Nick Rogers and an anonymous reviewer provided helpful comments on an earlier version of this paper. Marjorie Wilson's thorough editorial assistance also improved this manuscript. This research was supported by the British Council, Royal Society and the Industrial Association at RHUL. The XRF and both isotope laboratories at RHUL are University of London Intercollegiate facilities.

REFERENCES

Agar, R. A., Stacey, J. S. & Whitehouse, M. J., 1992. Evolution of the southern Afif terrane—a geochronologic study. *Directorate General of Mineral Resources Open File Report* **DGMR-OF-10-15**, 41 pp.

Aitchensen, S. J. & Forrest, A. H., 1994. Quantification of crustal contamination in open magmatic systems. *Journal of Petrology* **35,** 461–488.

Altherr, R., Henjes-Kunst, F. & Baumann, A., 1990. Asthenosphere versus lithosphere as possible sources for basaltic magmas erupted during formation of the Red Sea: constraints from Sr, Pb and Nd isotopes. *Earth and Planetary Science Letters* **96,** 269–286.

Ambraseys, N. N., Melville, C. P. & Adams, R. D., 1994. *The Seismicity of Egypt, Arabia and the Red Sea*. Cambridge University Press, 201 pp.

Baker, J. A., 1996. Stratigraphy, geochronology and geochemistry of Cenozoic volcanism in western Yemen. Ph.D. Thesis, University of London, 386 pp.

Baker, J. A., Thirlwall, M. F. & Menzies, M. A., 1996. Sr–Nd–Pb isotopic and trace element evidence for crustal contamination of plume-derived flood basalts: Oligocene flood volcanism in western Yemen. *Geochimica et Cosmochimica Acta* **60,** 2559–2581.

Bielski, M., 1982. M.Sc. Thesis, Hebrew University of Jerusalem.

Blusztajn, J., Hart, S. R., Shimizu, N. & McGuire, A. V., 1995. Trace element and isotopic characteristics of spinel peridotite xenoliths from Saudi Arabia. *Chemical Geology* **123,** 53–65.

Camp, V. E. & Roobol, M. J., 1989. The Arabian continental alkali basalt province: Part I. Evolution of Harrat Rahat, Kingdom of Saudi Arabia. *Geological Society of America Bulletin* **101,** 71–95.

Camp, V. E. & Roobol, M. J., 1992. Upwelling asthenosphere beneath western Arabia and its regional implications. *Journal of Geophysical Research* **97,** 15255–15271.

Camp, V. E., Roobol, M. J. & Hooper, P. R., 1991. The Arabian continental alkali basalt province: Part II. Evolution of Harrats Khaybar, Ithayn and Kura, Kingdom of Saudi Arabia. *Geological Society of America Bulletin* **103,** 363–391.

Camp, V. E., Roobol, M. J. & Hooper, P. R., 1992. The Arabian continental alkali basalt province: Part III. Evolution of Harrat Kishb, Kingdom of Saudi Arabia. *Geological Society of America Bulletin* **104,** 379–396.

Chaffey, D. J., Cliff, R. A. & Wilson, B. M., 1989. Characterisation of the St Helena magma source. *Geological Society of London Special Publication* **42,** 257–276.

Chazot, G., Menzies, M. A. & Harte, B., 1996. Determination of partition coefficients between apatite, clinopyroxene, amphibole, and melt in natural spinel lherzolites from Yemen: implications for wet melting of the lithospheric mantle. *Geochimica et Cosmochimica Acta* **60,** 423–437.

Cohen, R. S., O'Nions, R. K. & Dawson, J. B., 1984. Isotope geochemistry of xenoliths from East Africa: implications for development of mantle reservoirs and their interaction. *Earth and Planetary Science Letters* **68,** 209–220.

Condie, K. C., 1993. Chemical composition and evolution of the upper continental crust: contrasting results from surface samples and shales. *Chemical Geology* **104,** 1–37.

Cox, K. G., Charnley, N., Gill, R. C. O. & Parish, K. A., 1993. Alkali basalts from Shuqra, Yemen, magmas generated in the crust–mantle transition zone. *Geological Society of London Special Publication* **76,** 443–454.

Davidson, J. P. & Wilson, I. R., 1989. Evolution of an alkali basalt–trachyte suite from Jebel Marra volcano, Sudan, through assimilation and fractional crystallization. *Earth and Planetary Science Letters* **95,** 141–160.

Davison, I., Al-Kadasi, M., Al-Khirbash, S., Al-Subbary, A.-K., Baker, J., Blakey, S., Bosence, D., Dart, C., Heaton, R., McClay, K., Menzies, M., Nichols, G., Owen, L. & Yelland, A., 1994. Geological evolution of the south-eastern Red Sea rift margin: Republic of Yemen. *Geological Society of America Bulletin* **106,** 1474–1493.

Deniel, C., Vidal, P., Coulon, C., Vellutini, P.-J. & Piguet, P., 1994. Temporal evolution of mantle sources during continental rifting: the volcanism of Djibouti (Afar). *Journal of Geophysical Research* **99,** 2853–2869.

DePaolo, D. J., 1981. Trace element and isotopic effects of combined wallrock assimilation and fractional crystallization. *Earth and Planetary Science Letters* **53,** 189–202.

Duyverman, H. J., Harris, N. B. W. & Hawkesworth, C. J., 1982. Crustal accretion in the Pan-African: Nd and Sr isotope evidence from the Arabian shield. *Earth and Planetary Science Letters* **59,** 315–326.

Eiler, J. M., Farley, K. A., Valley, J. W., Stolper, E. M., Hauri, E. H. & Craig, H., 1995. Oxygen isotope evidence against bulk recycled sediment in the mantle sources of Pitcairn Island lavas. *Nature* **377,** 138–141.

Gallagher, K. & Hawkesworth, C. J., 1992. Dehydration melting and the generation of continental flood basalts. *Nature* **358,** 57–59.

Hamelin, B. & Allègre, C. J., 1988. Lead isotope study of orogenic lherzolite massifs. *Earth and Planetary Science Letters* **91,** 117–131.

Hart, S. R. & Davis, K. E., 1978. Nickel partitioning between olivine and silicate melt. *Earth and Planetary Science Letters* **40,** 203–219.

Hegner, E. & Pallister, J. S., 1989. Pb, Sr and Nd isotopic characteristics of Tertiary Red Sea rift volcanics from the central Saudi Arabian coastal plain. *Journal of Geophysical Research* **94,** 7749–7755.

Henjes-Kunst, F., Altherr, R. & Baumann, A., 1990. Evolution and composition of the lithospheric mantle underneath the western Arabian peninsula: constraints from Sr–Nd isotope systematics of mantle xenoliths. *Contributions to Mineralogy and Petrology* **105,** 460–472.

Kostopoulos, D. K. & James, S. D., 1992. Parameterisation of the melting regime of the shallow upper mantle and the effects of variable lithospheric stretching on mantle model stratification and trace element concentrations in magmas. *Journal of Petrology* **33,** 665–691.

Kruck, W., 1983. Geologic map of the Yemen Arab Republic, Sheet Sana'a, scale 1:250 000. Hannover, Germany: Federal Institute for Geosciences and Natural Resources.

Le Bas, M. J., Le Maitre, R. W., Streckeisen, A. & Zanettin, B., 1986. A chemical classification of volcanic rocks based on the total alkali–silica diagram. *Journal of Petrology* **27,** 745–750.

Manetti, P., Capaldi, G., Chiesa, S., Civetta, L., Conticelli, S., Gasparon, M., La Volpe, L. & Orsi, G., 1991. Magmatism of the eastern Red Sea margin in the northern part of Yemen from Oligocene to present. *Tectonophysics* **198,** 181–202.

Mattey, D. P. & Macpherson, C. G., 1993. High-precision oxygen isotope analysis of ferromagnesian minerals by laser fluorination. *Chemical Geology (Isotope Geoscience Section)* **105,** 305–318.

Mattey, D. P., Lowry, D. & Macpherson, C. G., 1994. Oxygen isotope composition of mantle peridotites. *Earth and Planetary Science Letters* **128,** 231–241.

McGuire, A. V. & Stern, R. J., 1993. Granulite xenoliths from Saudi Arabia: the lower crust of the late Precambrian Arabian–Nubian shield. *Contributions to Mineralogy and Petrology* **114,** 395–408.

McKenzie, D. P. & O'Nions, R. K., 1991. Partial melt distributions from inversion of rare earth element concentrations. *Journal of Petrology* **32,** 1021–1091.

Mooney, W. D., Gettings, M. E., Blank, H. R. & Healy, J. W., 1985. Saudi Arabian seismic deep refraction profile: a travel-time interpretation of crust and upper mantle structure. *Tectonophysics* **111,** 173–246.

Nakamura, N., 1974. Determination of REE, Ba, Mg, Na and K in carbonaceous and ordinary chondrites. *Geochimica et Cosmochimica Acta* **38,** 757–775.

Olafsson, M. & Eggler, D. H., 1983. Phase relations of amphibole, amphibole–carbonate, and phlogopite–carbonate peridotite: petrologic constraints on the asthenosphere. *Earth and Planetary Science Letters* **64,** 305–315.

Roeder, P. L. & Emslie, R. F., 1970. Olivine–liquid equilibrium. *Contributions to Mineralogy and Petrology* **90,** 275–289.

Rudnick, R. L. & Taylor, S. R., 1987. The composition and petrogenesis of the lower crust: a xenolith study. *Journal of Geophysical Research* **92,** 13981–14005.

Sack, R. O., Walker, D. & Carmichael, I. S. E., 1987. Experimental petrology of alkalic lavas: constraints on cotectics of multiple saturation in natural basic liquids. *Contributions to Mineralogy and Petrology* **96,** 1–23.

Schilling, J.-G., Kingsley, R. H., Hanan, B. B. & McCully, B. L., 1992. Nd–Sr–Pb isotopic variations along the Gulf of Aden: evidence for mantle plume–continental lithosphere interaction. *Journal of Geophysical Research* **97,** 10927–10966.

Shaw, D. M., 1970. Trace element fractionation during anatexis. *Geochimica et Cosmochimica Acta* **34,** 237–243.

Shaw, D. M., Gramer, J. J., Higgins, M. D. & Truscott, M. G., 1986. Composition of the Canadian shield and the continental crust of the earth. *Geological Society of London Special Publication* **24,** 275–282.

Stein, M. & Goldstein, S. L., 1996. From plume head to continental lithosphere in the Arabian–Nubian shield. *Nature* **382,** 773–778.

Stein, M. & Hofmann, A. W., 1992. Fossil plume head beneath the Arabian lithosphere? *Earth and Planetary Science Letters* **114,** 193–209.

Stein, M. & Hofmann, A. W., 1994. Mantle plumes and episodic crustal growth. *Nature* **372,** 63–68.

Sun, S.-s. & McDonough, W. F., 1989. Chemical and isotopic systematics of oceanic basalts: implications for mantle composition and processes. *Geological Society of London Special Publication* **42,** 313–345.

Taylor, S. R. & McLennan, S. M., 1985. *The Continental Crust: its Composition and Evolution*. London: Blackwell, 312 pp.

Thirlwall, M. F., 1991. Long-term reproducibility of multicollector Sr and Nd isotope ratio analyses. *Chemical Geology (Isotope Geoscience Section)* **94,** 85–104.

Thirlwall, M. F., Upton, B. G. J. & Jenkins, C., 1994. Interaction between continental lithosphere and the Iceland plume—Sr–Nd–Pb isotope chemistry of Tertiary basalts, NE Greenland. *Journal of Petrology* **35,** 839–879.

Vidal, P., Deniel, C., Vellutini, P. J., Piguet, P., Coulon, C., Vincent, J. & Audin, J., 1991. Changes of mantle sources in the course of a rift evolution: the Afar case. *Geophysical Research Letters* **18,** 1913–1916.

Volker, F., McCulloch, M. T. & Altherr, R., 1993. Submarine basalts from the Red Sea: new Pb, Sr and Nd isotopic data. *Geophysical Research Letters* **20,** 927–930.

Wallace, M. E. & Green, D. H., 1988. An experimental determination of primary carbonatite magma composition. *Nature* **335,** 343–346.

Weaver, B. L., 1991. The origin of ocean island basalt end-member compositions: trace element and isotopic constraints. *Earth and Planetary Science Letters* **104,** 381–397.

Weaver, B. L. & Tarney, J., 1984. Empirical approach to estimating the composition of the continental crust. *Nature* **310,** 575–577.

Windley, B. F., Whitehouse, M. J. & Ba-Bttat, M. A. O., 1996. Early Precambrian gneiss terranes and Pan-African island arcs in Yemen: crustal accretion of the eastern Arabian Shield. *Geology* **24,** 131–134.

Zindler, A. & Hart, S. R., 1986. Chemical geodynamics. *Annual Reviews of Earth and Planetary Science* **14,** 493–571.